GM 67278

Logistics and processing report, GEOTEM airborne electromagnetic survey, Deborah lake property

Documents complémentaires

Additional Files

Licence

License

Fugro Airborne Surveys

FUGRO

LOGISTICS AND PROCESSING REPORT
GEOTEM® Airborne Electromagnetic Survey

DEBORAH LAKE PROPERTY
QUÉBEC

Job No. 10408

Western Troy Capital Resources Inc.

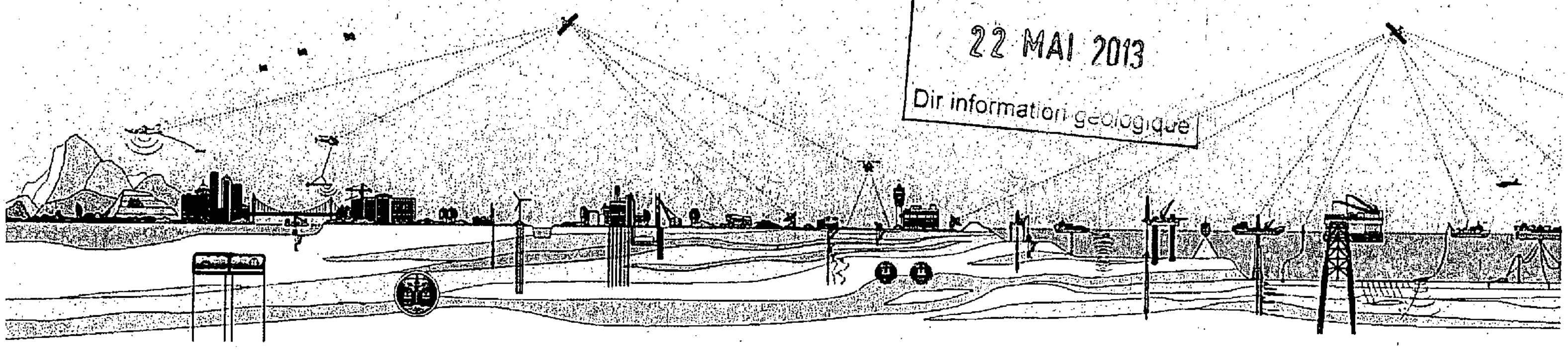

LOGISTICS AND PROCESSING REPORT
GEOTEM® AIRBORNE SURVEY
DEBORAH LAKE PROPERTY
QUÉBEC

JOB NO. 10408

Client: Western Troy Capital Resources Inc.
133 Avenue Road
3rd Floor
Toronto, Ontario
M5R 1N7

Date of Report: January, 2011

2191 Thurston Drive, Ottawa, Ontario K1G 6C9. Phone: (1-613) 731-9575, Fax: (1-613) 731-0453.

TABLE OF CONTENTS

APPENDICES

I

Introduction

Between December 10th and 11th, 2010 Fugro Airborne Surveys conducted a GEOTEM® airborne electromagnetic survey of the Deborah Lake Property on behalf of Western Troy Capital Resources Incorporated. Using Schefferville, Québec as the base of operations, a total of 697 line kilometres of data were collected using a Casa 212 modified aircraft (Figure 1).

The survey data were processed and compiled in the Fugro Airborne Surveys Ottawa office. The collected and processed data are presented on colour maps, and multi-parameter profiles. The following maps were produced: Tau of B-Field X Channels 10-30, Equivalent Delay Time Conductance from dB/dt Z-Coil Channel 01, Second Order Moment from Z-Coil, and Flight Path. In addition, digital archives of the raw and processed survey data in line format, and gridded EM data were delivered.

Figure 1: Specially modified Casa 212 aircraft used by Fugro Airborne Surveys.

II

Survey Operations

Location of the Survey Area

The Deborah Lake Property (Figure 2) was flown with Schefferville, Québec as the base of operations. A total of 78 traverse lines were flown ranging in length from 7 km to 13 km, with a spacing of 200 m between lines (100 m for the infill area) totalling 697 km for the complete survey.

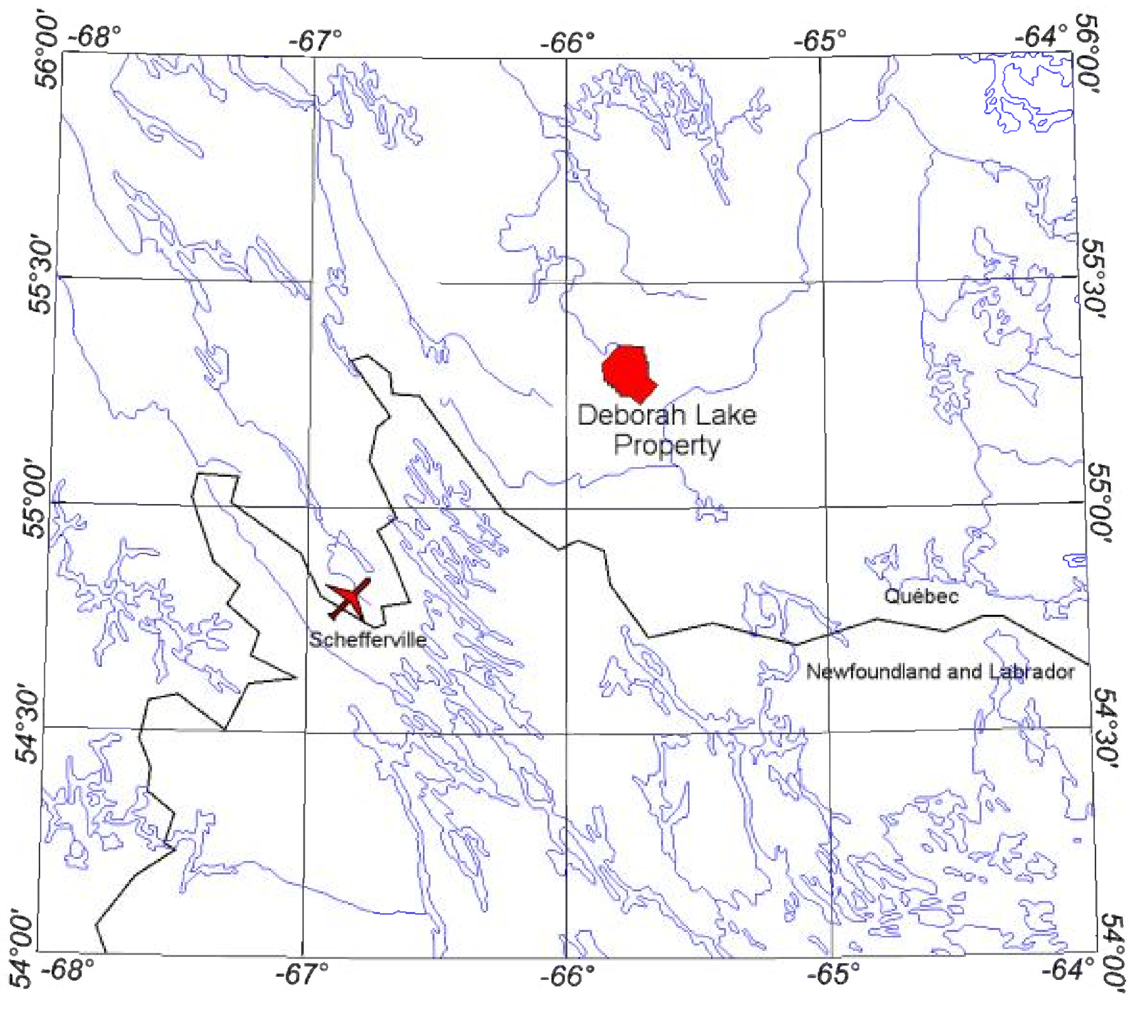

Figure 2: Survey location.

Aircraft and Geophysical On-Board Equipment

Aircraft:	Casa 212 (Twin Turbo Propeller)
Operator:	FUGRO AIRBORNE SURVEYS
Registration:	C-GDKM
Survey Speed:	125 knots / 145 mph / 65 m/s
Electromagnetic system:	GEOTEM® 30 channel Multi-coil System
Transmitter:	Vertical axis loop mounted on aircraft of 231 m^2
	Number of turns 6
	Nominal height above ground of 120 m
Receiver:	Multi-coil system (x, y and z) with a final recording rate of 4 samples per second, for the recording of 30 channels of x, y and z-coil data. The nominal height above ground is ~73 m, placed ~125 m behind the centre of the transmitter loop.
Base frequency:	30 Hz
Pulse width:	4044 μs
Pulse delay:	24 μs
Off-time:	12599 μs
Point value:	8.14 μs
Transmitter Current:	615 A
Dipole moment:	$8.5 \times 10^5 Am^2$

Figure 3: Mag and GEOTEM® Receivers

Figure 4: Modified Casa 212 in flight.

Table 1: Electromagnetic Data Windows.

Channel	Start (p)	End (p)	Width (p)	Start (ms)	End (ms)	Width (ms)	Mid (ms)
1	4	18	15	0.024	0.146	0.122	0.085
2	19	176	158	0.146	1.432	1.286	0.789
3	177	333	157	1.432	2.710	1.278	2.071
4	334	491	158	2.710	3.996	1.286	3.353
5	492	507	16	3.996	4.126	0.130	4.061
6	508	512	5	4.126	4.167	0.041	4.146
7	513	518	6	4.167	4.215	0.049	4.191
8	519	526	8	4.215	4.281	0.065	4.248
9	527	536	10	4.281	4.362	0.081	4.321
10	537	548	12	4.362	4.460	0.098	4.411
11	549	562	14	4.460	4.574	0.114	4.517
12	563	578	16	4.574	4.704	0.130	4.639
13	579	596	18	4.704	4.850	0.146	4.777
14	597	616	20	4.850	5.013	0.163	4.932
15	617	641	25	5.013	5.216	0.203	5.115
16	642	671	30	5.216	5.461	0.244	5.339
17	672	706	35	5.461	5.745	0.285	5.603
18	707	746	40	5.745	6.071	0.326	5.908
19	747	791	45	6.071	6.437	0.366	6.254
20	792	841	50	6.437	6.844	0.407	6.641
21	842	901	60	6.844	7.332	0.488	7.088
22	902	971	70	7.332	7.902	0.570	7.617
23	972	1051	80	7.902	8.553	0.651	8.228
24	1052	1141	90	8.553	9.285	0.732	8.919
25	1142	1241	100	9.285	10.099	0.814	9.692
26	1242	1361	120	10.099	11.076	0.977	10.588
27	1362	1501	140	11.076	12.215	1.139	11.646
28	1502	1661	160	12.215	13.517	1.302	12.866
29	1662	1841	180	13.517	14.982	1.465	14.250
30	1842	2048	207	14.982	16.667	1.685	15.824

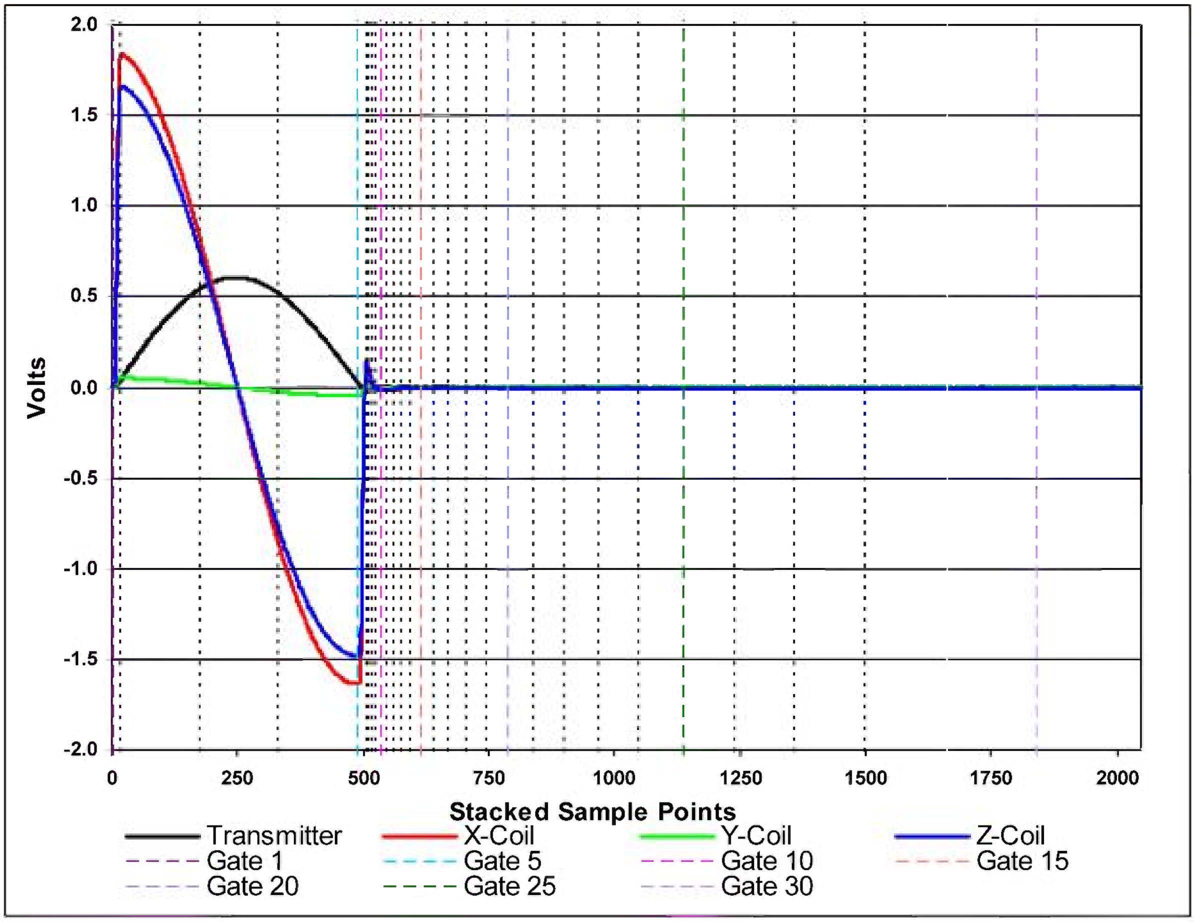

Figure 5: GEOTEM® Waveform and response with gate centres showing positions in sample points.

Digital Acquisition:	FUGRO AIRBORNE SURVEYS GEODAS SYSTEM.
Barometric Altimeter:	Rosemount 1241M, sensitivity 1 ft, 0.5 sec recording interval.
Radar Altimeter:	King, accuracy 2%, sensitivity 1 ft, range 0 to 2500 ft, 0.5 sec recording interval.
Camera:	Panasonic colour video, super VHS, model WV-CL302.
Electronic Navigation:	NovAtel OEM4, 1 sec recording interval, with a resolution of 0.00001 degree and an accuracy of ±5m.

Base Station Equipment

GPS Receiver:	NovAtel OEM4, measuring all GPS channels, for up to 12 satellites.
Computer:	Laptop, Pentium model or better.
Data Logger:	CF1, SBBS (single board base station).

Field Office Equipment

Computer:	Dell Laptop.
Printer:	Portable printer.
DVD writer Drive:	Internal DVD+RW format.
Hard Drives:	Internal hard drive + two external hard drives for redundant backups.

Survey Specifications

Traverse Line Direction:	045° - 225°
Traverse Line Spacing:	200 m
Traverse Line Spacing (infill):	100 m
Navigation:	Real-time differential GPS. Traverse and tie line spacing was not to exceed the nominal by > 50 m for more than 3 km.
Altitude:	The survey was flown at a mean terrain clearance of 120 m. Altitude was not to exceed 140 m over 3 km.
EM Noise Levels:	The noise envelope on the last raw electromagnetic dB/dt X- and Z-coil channel was not to exceed ± 3500 pT/s over a distance greater than 3 km.

Field Crew

Pilots:	T. Gaillot, P. MacNeil
Electronics Operator:	A. Proulx

Production Statistics

Flying dates:	December 10th – December 11th, 2010
Total production:	697 line kilometres
Number of production flights:	3
Days lost weather:	0

III

Quality Control and Compilation Procedures

Important checks were performed during the data acquisition stage to ensure that the data quality was in keeping with the survey specifications. The following outlines the Quality Control measures conducted throughout the acquisition phase of the survey.

Initial Field QC

At the completion of each day's flying an initial review of the data was performed in the field. This process was primarily to ensure all the equipment was functioning properly and enables the crew to immediately ascertain that production can resume the following day. This process does not necessarily determine if the data were within specifications. Priority was given to getting the data back to the office where a more thorough analysis of the data was performed. A list of the steps of the initial field review of the data follows:

1) All digital files were confirmed to be readable and free of defects.
2) The integrity of the airborne electromagnetic data was checked through statistical analysis and graphically viewed in profile form. Any null values or unreasonable noise levels were identified.
3) All altimeter and positional data were checked for any inconsistency, invalid values and spikes.
4) The base station files were examined for validity and continuity. The data extent was confirmed to cover the entire acquisition period.
5) The diurnal data were examined for any noise events or spiking.
6) Flight path video files were visually checked for quality and to confirm the full coverage for the survey flight.
7) Duplicate backups of all digital files were created.

Transmission of Data from Field to Office

At the completion of each day's flying the raw data was uploaded to a secure FTP site. This enabled the office processing staff to immediately conduct more thorough data quality checks and start the processing with a minimum duplication of procedures or loss of time. This also enabled the direct supervision and involvement by senior processors and the availability of a greater depth of knowledge to be applied to any problems with the minimum of delay.

IV

Data Processing

Flight Path Recovery

GPS Recovery: GPS positions recalculated from the recorded raw range data, and differentially corrected.

Projection: Universal Transverse Mercator (UTM Zone 20N)

Datum: NAD83

Central meridian: 63° West

False Easting: 500000 metres

False Northing: 0 metres

Scale factor: 0.9996

Altitude Data

Noise editing: Alfatrim median filter used to eliminate the highest and lowest values from the statistical distribution of a 5 point sample window for the GPS elevation, and the two highest and lowest values from a 9 point sample window for the radar and barometric altimeters.

Gridding: The data were gridded using a bi-directional routine with a grid cell size of 50 m.

Electromagnetics

dB/dt data

Lag correction: 3.75 s

Data correction: The x, y and z-coil data were processed from the 30 raw channels recorded at 4 samples per second.

The following processing steps were applied to the dB/dt data from all coil sets:

a) The data from channels 1 to 5 (on-time) and 6 to 30 (off-time) were corrected for drift in flight form (prior to cutting the recorded data back to the correct line limits) by passing a low order polynomial function through the baseline minima along each channel, via a graphic screen display;

b) The data were edited for residual spheric spikes by examining the decay pattern of each individual EM transient. Bad decays (i.e. not fitting a normal exponential function) were deleted and replaced by interpolation;

c) Noise filtering was done using an adaptive filter technique based on time domain triangular operators. Using a 2nd difference value to identify changes in gradient along each channel, minimal filtering (3 point convolution) is applied over the peaks of the anomalies, ranging in set increments up to a maximum amount of filtering in the resistive background areas (21 points for both the x-coil and the z-coil data);

d) The filtered data from the x, y and z-coils were then re-sampled to a rate of 5 samples per second and combined into a common file for archiving.

B-field data

Processing steps: The processing of the B-Field data stream is very similar to the processing for the regular dB/dt data. The lag adjustment used was the same, followed by:

1) Drift adjustments;
2) Spike editing for spheric events;
3) Correction for coherent noise. By nature, the B-Field data will contain a higher degree of coherency of the noise that automatically gets eliminated (or considerably attenuated) in the regular dB/dt, since this is the time derivative of the signal;
4) Final noise filtering with an adaptive filter.

Note: The introduction of the B-Field data stream, as part of the GEOTEM® system, provides the explorationist with a more effective tool for exploration in a broader range of geological environments and for a larger class of target priorities.

The advantage of the B-Field data compared with the normal voltage data (dB/dt) are as follows:

1. A broader range of target conductance that the system is sensitive to. (The B-Field is sensitive to bodies with conductance as great as 100,000 siemens);
2. Enhancement of the slowly decaying response of good conductors;
3. Suppression of rapidly decaying response of less conductive overburden;
4. Reduction in the effect of spherics on the data;
5. An enhanced ability to interpret anomalies due to conductors below thick conductive overburden;
6. Reduced dynamic range of the measured response (easier data processing and display).

Figure 6 displays the calculated vertical plate response for the GEOTEM® signal for the dB/dt and B-Field. For the dB/dt response, you will note that the amplitude of the early channel peaks at about 25 siemens, and the late channels at about 250 siemens. As the conductance exceeds 1000 siemens the response curves quickly roll back into the noise level. For the B-Field response, the early channel amplitude peaks at about 80 siemens and the late channel at about 550 siemens. The projected extension of the graph in the direction of increasing conductance, where the response

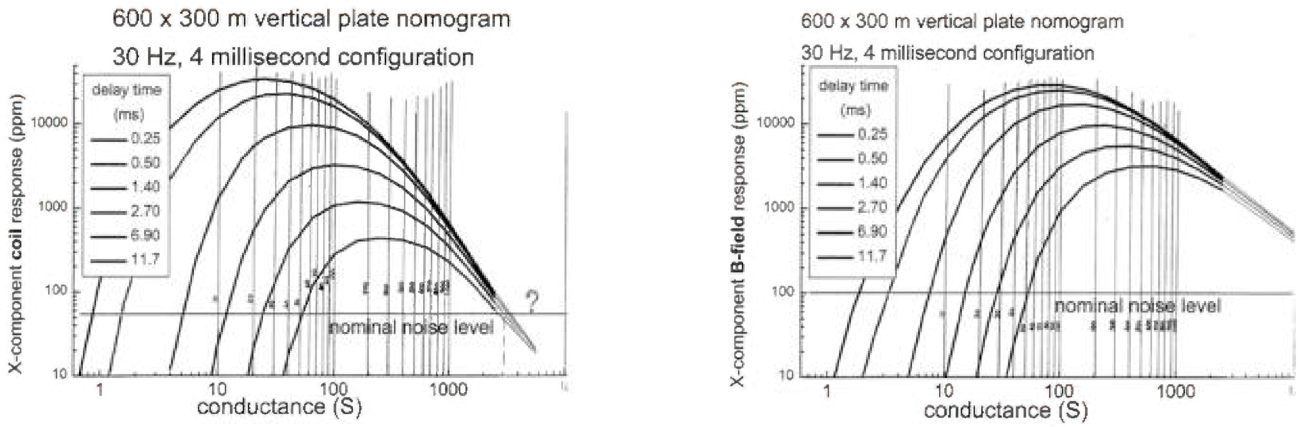

Figure 6: dB/dt vertical plate nomogram (left), B-field vertical plate nomogram (right).

would roll back into the noise level, would be close to 100,000 siemens. Thus, a strong conductor, having a conductance of several thousand siemens, would be difficult to interpret on the dB/dt data, since the response would be mixed in with the background noise. However, this strong conductor would stand out clearly on the B-Field data, although it would have an unusual character, being a moderate to high amplitude response, exhibiting almost no decay.

In theory, the response from a super conductor (50,000 to 100,000 siemens) would be seen on the B-Field data as a low amplitude, non-decaying anomaly, not visible in the off-time channels of the dB/dt stream. Caution must be exercised here, as this signature can also reflect a residual noise event in the B-Field data. In this situation, careful examination of the dB/dt on-time (in-pulse) data is required to resolve the ambiguity. If the feature were strictly a noise event, it would not be present in the dB/dt off-time data stream. This would locate the response at the resistive limit, and the mid in-pulse channel (normally identified as channel 3) would reflect little but background noise, or at best a weak negative peak. If, on the other hand, the feature does indeed reflect a superconductor, then this would locate the response at the inductive limit. In this situation, channel 3 of the dB/dt stream will be a mirror image of the transmitted pulse, i.e. a large negative.

Coil Oscillation Correction

The electromagnetic receiver sensor is housed in a bird, which is towed behind the aircraft using a cable. Any changes in airspeed of the aircraft, variable crosswinds, or other turbulence will result in the bird swinging from side to side. This can result in the induction sensors inside the bird rotating about their mean orientation. The rotation is most marked when the air is particularly turbulent. The changes in orientation result in variable coupling of the induction coils to the primary and secondary fields. For example, if the sensor that is normally aligned to measure the x-axis response pitches upward, it will be measuring a response that will include a mixture of the X and Z-component responses. The effect of coil oscillation on the data increases as the signal from the ground (conductivity) increases and may not be noticeable when flying over areas which are generally resistive. This becomes more of a concern when flying over highly conductive ground.

Using the changes in the coupling of the primary field, it is possible to estimate the pitch, roll and yaw of the receiver sensors. In the estimation process, it is assumed that a smoothed version of the primary field represents the primary field that would be measured when the sensors are in the mean orientation. The orientations are estimated using a non-linear inversion procedure, so erroneous orientations are sometimes obtained. These are reviewed and edited to insure smoothly varying values of orientations. These orientations can then be used to unmix the measured data to generate a response that would be measured if the sensors were in the correct orientation. For more information on this procedure please refer to *Advances in Time-Domain EM Technology* published in Proceedings of Exploration 97; Fourth Decennial International Conference on Mineral Exploration by R. Smith and P. Annan.

For the present dataset, the data from all 30 channels of dB/dt and B-Field parameters have been corrected for coil oscillation.

Decay Constant (TAU)

The decay constant values are obtained by fitting the channel data from either the complete off-time signal of the decay transient or only a selected portion of it (as defined by specific channels) to a single exponential of the form

$$Y = A\,e^{-t/\tau}$$

where **A** is amplitude at time zero, **t** is time in microseconds and τ is the decay constant, expressed in microseconds. A semi-log plot of this exponential function will be displayed as a straight line, the slope of which will reflect the rate of decay and therefore the strength of the conductivity. A slow rate of decay, reflecting a high conductivity, will be represented by a high decay constant.

As a single parameter, the decay constant provides more useful information than the amplitude data of any given single channel, as it indicates not only the peak position of the response but also the relative strength of the conductor. It also allows better discrimination of conductive axes within a broad formational group of conductors.

For the present dataset, the decay constant was calculated by fitting the X-coil response from channels 10 to 30 (mean delay times of 343 to 11756 µsec after turn-off) of the B-Field component to the exponential function.

Equivalent Delay Time Conductance

Fugro has developed an algorithm that converts the response in any measurement window, or range of windows, into an apparent conductance. This is performed using a look-up table that contains the response at a range of conductances and altimeter heights based on the Horizontal Thin Sheet model.

The apparent conductance for the present dataset was calculated using dB/dt Z-Coil channel 01 to provide the maximum information on the near-surface conductivity of the ground which, when combined with the magnetic signature, provides good geological mapping.

Moments of the Impulse Response

For this dataset, the moments of the impulse response are a good way of highlighting a number of features in the dataset. The n^{th} moment is defined as

$$M^n = \int_0^\infty t^n I(t)\,dt\,,$$

where $I(t)$ is the impulse response.

One advantage of the moments is that they place different emphasis on different parts of the transient. The low-order moments (n=1) place emphasis on the early-time data and this reflects the near-surface information. The higher order moments (n=2,3...) place emphasis on the late-time data (or deeper information). For a more detailed description of moments please refer to *The Moments of the Impulse Response: A new paradigm for the Interpretation of Transient Electromagnetic Data* published in Geophysics, Vol. 67, No. 4; 1095-1103 by R. Smith and T. Lee.

Another advantage of the moments is that these quantities can be easily converted to conductivity or conductance. For more details on this transformation please refer to *Approximate Apparent Conductance (or Conductivity) from the Realisable Moments of the Impulse Response* published in Geophysics, 2005, Vol. 70; G29-G32 by R. Smith et al.

The moments can also be used to characterize discrete conductors by using a small sphere model to determine the depth, dip, conductivity etc. For more details on this model please refer to *The Impulse-Response Moments of a Conductive Sphere in a Uniform Field, A Versatile and Efficient Electromagnetic Model* published in Exploration Geophysics, 2001, Vol. 32, 113-118 by R. Smith and T. Lee.

For the present dataset the 2^{nd} Order Moment was calculated from the B-Field Z-Coil data.

V

Final Products

Digital Archives

Line and grid data in the form of an ASCII text file (*.xyz), Geosoft database (*.gdb) and Geosoft grids (*.grd) have been written to DVD. The formats and layouts of these archives are further described in Appendix E (Data Archive Description). Hardcopies of all maps have been created as outlined below.

Maps

Scale:	1:25,000
Parameters:	Decay Constant (Tau) derived from B-Field X-Coil Channels 10-30 Equivalent Delay Time Conductance derived from dB/dt Z-Coil Channel 01 2nd Order Moment derived from B-Field Z-Coil
Media/Copies:	1 Paper & 2 digital (Geosoft MAP format)

Profile Plots

Scale:	1:25,000
Parameters:	Multi-channel presentation with 23 channels of both dB/dt and B-field X and Z-coil, Residual Magnetic Intensity, Calculated Magnetic Vertical Gradient, Radar Altimeter, GPS Altitude, EM Primary Field, and Hz Monitor.
Media/Copies:	2 Digital of Each Line (PNG format)

Report

Media/Copies:	2 Paper & 2 digital (PDF format)

Appendix A

Fixed-Wing Airborne Electromagnetic Systems

FIXED-WING AIRBORNE ELECTROMAGNETIC SYSTEMS

General

The operation of a towed-bird time-domain electromagnetic system (EM) involves the measurement of decaying secondary electromagnetic fields induced in the ground by a series of short current pulses generated from an aircraft-mounted transmitter. Variations in the decay characteristics of the secondary field (sampled and displayed as windows) are analyzed and interpreted to provide information about the subsurface geology. The response of such a system utilizing a vertical-axis transmitter dipole and a multi-component receiver coil has been documented by various authors including Smith and Keating (1991, Geophysics v.61, p. 74-81).

A number of factors combine to give the fixed-wing platforms excellent signal-to-noise ratio and depth of penetration: 1) the principle of sampling the induced secondary field in the absence of the primary field (during the “off-time”), 2) the large separation of the receiver coils from the transmitter, 3) the large dipole moment and 4) the power available from the fixed wing platform. Such a system is also relatively free of noise due to air turbulence. However, also sampling in the “on-time” can result in excellent sensitivity for mapping very resistive features and very conductive features, and thus mapping the geology (Annan et al., 1991, Geophysics v.61, p. 93-99). The on-time and off-time parts of the half-cycle waveform are shown in Figure 1.

Through free-air model studies using the University of Toronto's Plate and Layered Earth programs it may be shown that the “depth of investigation” depends upon the geometry of the target. Typical depth limits would be 400 m below surface for a homogeneous half-space, 550 m for a flat-lying inductively thin sheet or 300 m for a large vertical plate conductor. These depth estimates are based on the assumptions that the overlying or surrounding material is resistive.

The method also offers very good discrimination of conductor geometry. This ability to distinguish between flat-lying and vertical conductors combined with excellent depth penetration results in good differentiation of bedrock conductors from surficial conductors (Appendix C).

Methodology

The Fugro time-domain fixed-wing electromagnetic systems (GEOTEM® and MEGATEM®) incorporate a high-speed digital EM receiver. The primary electromagnetic pulses are created by a series of discontinuous sinusoidal current pulses fed into a three- or six-turn transmitting loop surrounding the aircraft and fixed to the nose, tail and wing tips. The base frequency rate is selectable: 25, 30, 75, 90, 125, 150, 225 and 270 Hz. The length of the pulse can be tailored to suit the targets. Standard pulse widths available are 0.6, 1.0, 2.0 and 4.0 ms. The available off-time can be selected to be as great as 16 ms. The dipole moment depends on the pulse width, base frequency and aircraft used on the survey. Example pulse widths and off-time windows at different base frequencies are shown on Figure 2. The specific dipole moment, waveform and gate settings for this survey are given in the main body of the report.

The receiver is a three-axis (x, y, z) induction coil. In the fixed-wing systems, this is towed by the aircraft on a 135-metre cable. The tow cable is non-magnetic, to reduce noise levels. The usual mean terrain clearance for the aircraft is 120 m with the EM bird being situated nominally 50 m below and 130 m behind the aircraft (see Figure 3).
Each primary pulse causes decaying eddy currents in the ground to produce a secondary magnetic field. This secondary magnetic field, in turn, induces a voltage in the receiver coils, which is the

electromagnetic response. Good conductors decay slowly, while poor conductors more rapidly (see Figure 1).

The measured signals pass through anti-aliasing filters and are then digitized with an A/D converter at sampling rates of up to 80 kHz. The digital data flows from the A/D converter into an industrial-grade computer where the data are processed to reduce the noise.

Operations, which are carried out in the receiver, are:

1. *Primary-field removal:* In addition to measuring the secondary response from the ground, the receiver sensor coils also measure the primary response from the transmitter. During flight, the bird position and orientation changes slightly, and this has a very strong effect on the magnitude of the total response (primary plus secondary) measured at the receiver coils. The variable primary field response is distracting because it is unrelated to the ground response. The primary field can be measured by flying at an altitude such that no ground response is measurable. These calibration signals are used to define the shape of the primary waveform. By definition this primary field includes the response of the current in the transmitter loop plus the response of any slowly decaying eddy currents induced in the aircraft. We assume that the shape of the primary will be unchanged as the bird position changes, but that the amplitude will vary. The primary-field-removal procedure involves solving for the amplitude of the primary field in the measured response and removing this from the total response to leave a secondary response. Note that this procedure removes any ("in-phase") response from the ground that has the same shape as the primary field. For more details on the primary-field removal procedure please refer to *On removing the primary field from fixed-wing time-domain airborne electromagnetic data: some consequences for quantitative modeling, estimating bird position and detecting perfect conductors* published in Geophysical Prospecting, 2001, Vol. 49; 405-416 by R. Smith.

2. *Digital Stacking:* Stacking is carried out to reduce the effect of broadband noise on the data.

3. *Windowing of data*: The digital receiver samples the secondary and primary electromagnetic field at 512, 1024, or 2048 points per EM pulse and windows the signal in up to 20 time gates whose centres and widths are software selectable and which may be placed anywhere within or outside the transmitter pulse. This flexibility offers the advantage of arranging the gates to suit the goals of a particular survey, ensuring that the signal is appropriately sampled through its entire dynamic range. Example off-time windows are shown on Figure 1.

4. *Power Line Filtering:* Digital comb filters are applied to the data during real-time processing to remove power line interference while leaving the EM signal undisturbed. The RMS power line voltage (at all harmonics in the receiver passband) are computed, displayed and recorded for each data stack.

5. *Primary Field:* The primary field at the towed sensor is measured for each stack and recorded as a separate data channel to assess the variation in coupling between the transmitter and the towed sensor induced by changes in system geometry.

6. *Earth Field Monitor:* A monitor of sensor coil motion noise induced by coil motion in the Earth's magnetic field is also extracted in the course of the real-time digital processing. This information is also displayed on the real-time chart as well as being recorded for post-survey diagnostic processes.

7. *Noise/Performance:* A monitor computes the RMS signal level on an early off-time window over a running 10-second window. This monitor provides a measure of noise levels in areas of low ground response. This information is printed at regular intervals on the side of the flight record and is recorded for every data stack.

One of the major roles of the digital receiver is to provide diagnostic information on system functions and to allow for identification of noise events, such as spherics, which may be selectively removed from the EM signal. The high digital sampling rate yields maximum resolution of the secondary field.

System Hardware

The airborne EM system consists of the aircraft, the on-board hardware, and the software packages controlling the hardware. The software packages in the data acquisition system and in the EM receiver were developed in-house, as were, certain elements of the hardware (transmitter, system timing clock, towed-bird sensor system).

Transmitter System

The transmitter system drives high-current pulses of an appropriate shape and duration through the coils mounted on the aircraft.

System Timing Clock

This subsystem provides appropriate timing signals to the transmitter, and also to the analog-to-digital converter, in order to produce output pulses and capture the ground response. All systems are synchronized to GPS time.

Towed-Bird System

A three-axis induction coil sensor is mounted inside a towed bird, which is typically 50 metres below and 130 metres behind the aircraft.

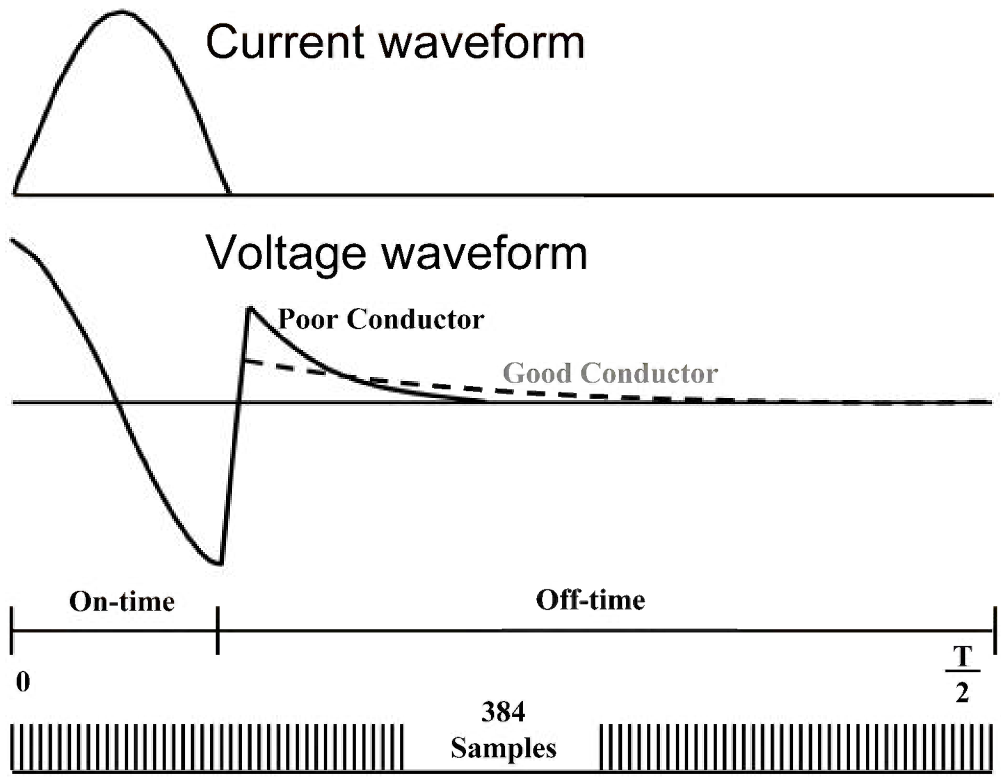

Figure 1. The waveforms and data sampling throughout the transmitter on and off-time.

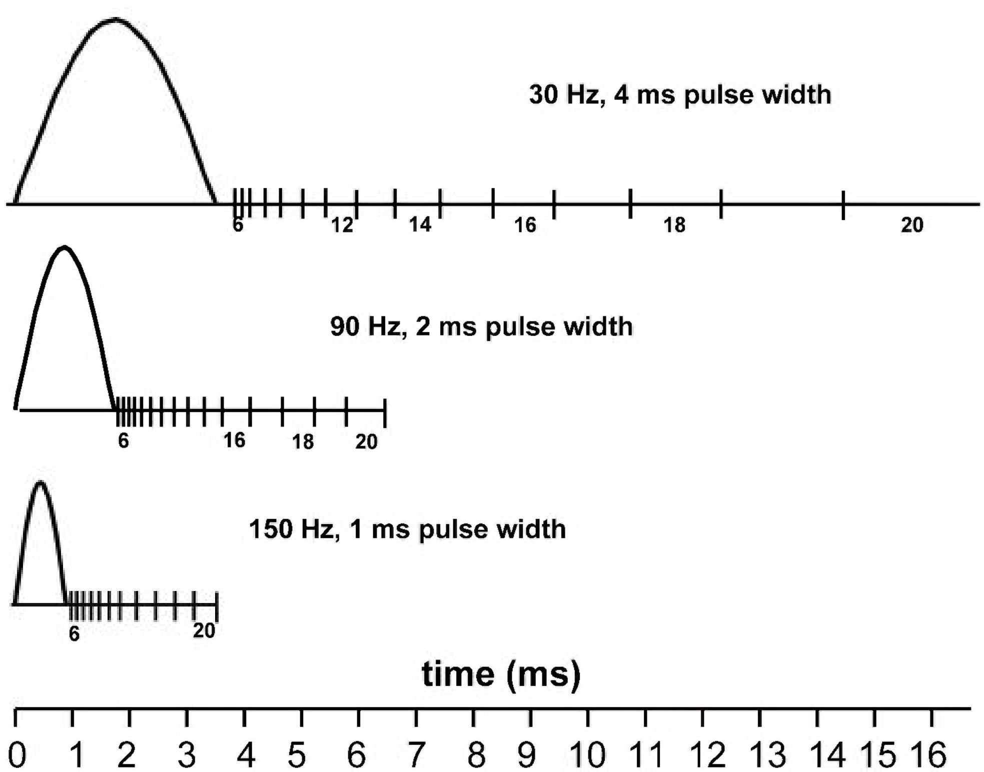

Figure 2. Pulse width and measurement windows for 150, 90 and 30 Hz base frequencies.

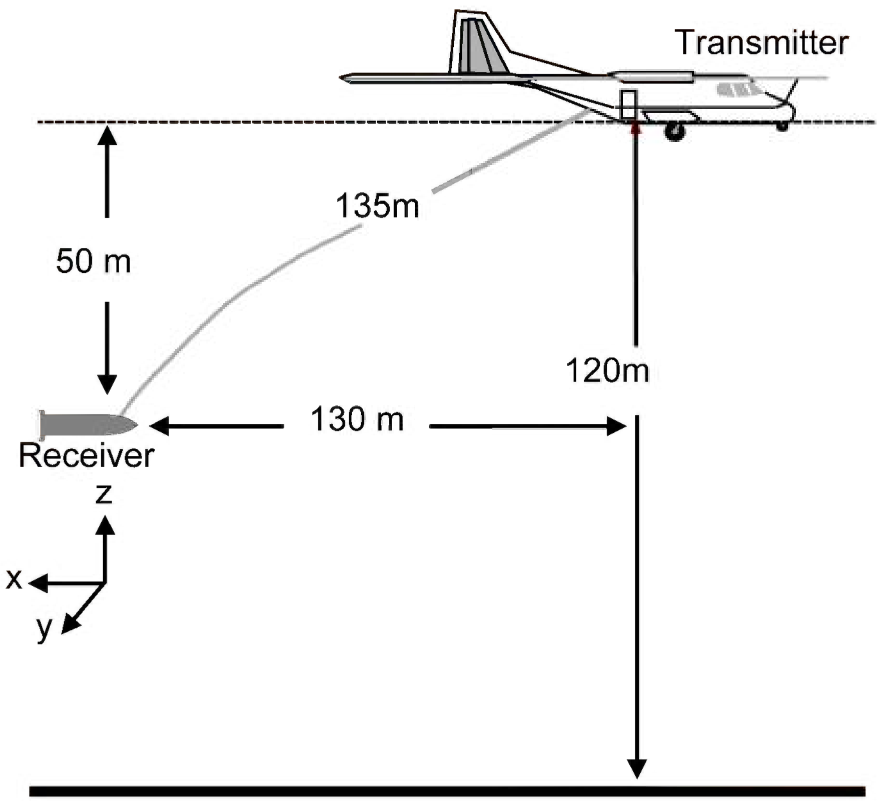

Figure 3. Nominal geometry of the fixed-wing electromagnetic system.

Appendix B

Airborne Transient EM Interpretation

Interpretation of transient electromagnetic data

Introduction

The basis of the transient electromagnetic (EM) geophysical surveying technique relies on the premise that changes in the primary EM field produced in the transmitting loop will result in eddy currents being generated in any conductors in the ground. The eddy currents then decay to produce a secondary EM field that may be sensed in the receiver coil.

MEGATEM® and GEOTEM® are airborne transient (or time-domain) towed-bird EM systems incorporating a high-speed digital receiver which records the secondary field response with a high degree of accuracy. Most often the earth's total magnetic field is recorded concurrently.

Although the approach to interpretation varies from one survey to another depending on the type of data presentation, objectives and local conditions, the following generalizations may provide the reader with some helpful background information.

The main purpose of the interpretation is to determine the probable origin of the responses detected during the survey and to suggest recommendations for further exploration. This is possible through an objective analysis of all characteristics of the different types of responses and associated magnetic anomalies, if any. If possible the airborne results are compared to other available data. Certitude is seldom reached, but a high probability is achieved in identifying the causes in most cases. One of the most difficult problems is usually the differentiation between surface conductor responses and bedrock conductor responses.

Types of Conductors

Bedrock Conductors

The different types of bedrock conductors normally encountered are the following:

1. *Graphites*. Graphitic horizons (including a large variety of carbonaceous rocks) occur in sedimentary formations of the Precambrian as well as in volcanic tuffs, often concentrated in shear zones. They correspond generally to long, multiple conductors lying in parallel bands. They have no magnetic expression unless associated with pyrrhotite or magnetite. Their conductivity is variable but generally high.

2. *Massive sulphides*. Massive sulphide deposits usually manifest themselves as short conductors of high conductivity, often with a coincident magnetic anomaly. Some massive sulphides, however, are not magnetic, others are not very conductive (discontinuous mineralization or sphalerite), and some may be located among formational conductors so that one must not be too rigid in applying the selection criteria.

   In addition, there are syngenetic sulphides whose conductive pattern may be similar to that of graphitic horizons but these are generally not as prevalent as graphites.

3. *Magnetite and some serpentinized ultrabasics*. These rocks are conductive and very magnetic.

4. *Manganese oxides*. This mineralization may give rise to a weak EM response.

Surficial Conductors

1. Beds of clay and alluvium, some swamps, and brackish ground water are usually poorly conductive to moderately conductive.

2. Lateritic formations, residual soils and the weathered layer of the bedrock may cause surface anomalous zones, the conductivity of which is generally low to medium but can occasionally be high. Their presence is often related to the underlying bedrock.

Cultural Conductors (Man-Made)

3. *Power lines*. These frequently, but not always, produce a conductive type of response. In the case when the power line comb filter does not remove the radiated field, the anomalous response can exhibit phase changes between different windows. In the case of current induced by the EM system in a grounded wire, or steel pylon, the anomaly may look very much like a bedrock conductor.

4. *Grounded fences or pipelines*. These will invariably produce responses much like a bedrock conductor. Whenever they cannot be identified positively, a ground check is recommended.

5. *General culture*. Other localized sources such as certain buildings, bridges, irrigation systems, tailings ponds etc., may produce EM anomalies. Their instances, however, are rare and often they can be identified on the visual path recovery system.

Analysis of the Conductors

The conductance of a plate is generally estimated assuming the plate is vertical and 600 m by 300 m. Hence the conductance alone is not generally a decisive criterion in the analysis of a conductor. In particular, one should note:

- Its shape and size,
- All local variations of characteristics within a conductive zone,
- Any associated geophysical parameter (e.g. magnetics),
- The geological environment,
- The structural context, and
- The pattern of surrounding conductors.

The first objective of the interpretation is to classify each conductive zone according to one of the three categories which best defines its probable origin. The categories are cultural, surficial and bedrock. A second objective is to assign to each zone a priority rating as to its potential as an economic prospect.

Bedrock Conductors

This category comprises those anomalies that cannot be classified according to the criteria established for cultural and surficial responses. It is difficult to assign a universal set of values that typify bedrock conductivity because any individual zone or anomaly might exhibit some, but not all, of these values and still be a bedrock conductor. The following criteria are considered indicative of a bedrock conductor:

1. An intermediate to high conductivity identified by a response with slow decay, with an anomalous response present in the later windows.

2. For vertical conductors, the anomaly should be narrow, relatively symmetrical, with a well-defined x-component peak.

3. If the conductor is thin, the response should show the characteristics evident in Figures 2 to 4. These figures illustrate how the response varies as a function of the flight direction for three bodies with different dips. The alternating character of the response as a result of line direction can be diagnostic of conductor geometry.

4. A small to intermediate amplitude. Large amplitudes are normally associated with surficial conductors. The amplitude varies according to the depth of the source.

5. A degree of continuity of the EM characteristics across several lines.

6. An associated magnetic response of similar dimensions. One should note, however, that those magnetic rocks that weather to produce a conductive upper layer would possess this magnetic association. In the absence of one or more of the characteristics defined in 1, 2, 3, 4 and 5, the related magnetic response cannot be considered significant.

Most obvious bedrock conductors occur in long, relatively monotonous, sometimes multiple zones following formational strike. Graphitic material is usually the most probable source. Massive syngenetic sulphides extending for many kilometres are known in nature but, in general, they are not common. Long formational structures associated with a strong magnetic expression may be indicative of banded iron formations.

In summary, a bedrock conductor reflecting the presence of a massive sulphide would normally exhibit the following characteristics:

- A high conductivity,
- A good anomaly shape (narrow and well-defined peak),
- A small to intermediate amplitude,
- An isolated setting,
- A short strike length (in general, not exceeding one kilometre), and
- Preferably, with a localized magnetic anomaly of matching dimensions.

Surficial Conductors

This term is used for geological conductors in the overburden, either glacial or residual in origin, and in the weathered layer of the bedrock. Most surficial conductors are probably caused by clay minerals. In some environments the presence of salts will contribute to the conductivity. Other possible electrolytic conductors are residual soils, swamps, brackish ground water and alluvium such as lake or river-bottom deposits, flood plains and estuaries.

Normally, most surficial materials have low to intermediate conductivity so they are not easily mistaken for highly conductive bedrock features. Also, many of them are wide and their anomaly shapes are typical of broad horizontal sheets.

When surficial conductivity is high it is usually still possible to distinguish between a horizontal plate (more likely to be surficial material) and a vertical body (more likely to be a bedrock source) thanks to the asymmetry of the fixed-wing system responses observed at the edges of a broad conductor when flying adjacent lines in opposite directions. The configuration of the system is such that the response recorded at the leading edge is more pronounced than that registered at the trailing edge. Figure 1 illustrates the "edge effect". In practice there are many variations on this very diagnostic phenomenon.

One of the more ambiguous situations as to the true source of the response is when surface conductivity is related to bedrock lithology as for example, surface alteration of an underlying bedrock unit. At times, it is also difficult to distinguish between a weak conductor within the bedrock (e.g. near-massive sulphides) and a surficial source.

In the search for massive sulphides or other bedrock targets, surficial conductivity is generally considered as interference but there are situations where the interpretation of surficial-type conductors is the primary goal. When soils, weathered or altered products are conductive, and in-situ, the responses are a very useful aid to geologic mapping. Shears and faults are often identified by weak, usually narrow, anomalies.

Analysis of surficial conductivity can be used in the exploration for such features as lignite deposits, kimberlites, palaeochannels and ground water. In coastal or arid areas, surficial responses may serve to define the limits of fresh, brackish and salty water.

Cultural Conductors

The majority of cultural anomalies occurs along roads and is accompanied by a response on the power line monitor. (This monitor is set to 50 or 60 Hz, depending on the local power grid.) In some cases, the current induced in the power line results in anomalies that could be mistaken for bedrock responses. There are also some power lines that have no response whatsoever.

The power line monitor, of course, is of great assistance in identifying cultural anomalies of this type. It is important to note, however, that geological conductors in the vicinity of power lines may exhibit a weak response on the monitor because of current induction via the earth.

Fences, pipelines, communication lines, railways and other man-made conductors can give rise to responses, the strength of which will depend on the grounding of these objects.

Another facet of this analysis is the line-to-line comparison of anomaly character along suspected man-made conductors. In general, the amplitude, the rate of decay, and the anomaly width should not vary a great deal along any one conductor, except for the change in amplitude related to terrain clearance variation. A marked departure from the average response character along any given feature gives rise to the possibility of a second conductor.

In most cases a visual examination of the site will suffice to verify the presence of a man-made conductor. If a second conductor is suspected the ground check is more difficult to accomplish. The object would be to determine if there is (i) a change in the man-made construction, (ii) a difference in the grounding conditions, (iii) a second cultural source, or (iv) if there is, indeed, a geological conductor in addition to the known man-made source.

The selection of targets from within extensive (formational) belts is much more difficult than in the case of isolated conductors. Local variations in the EM characteristics, such as in the amplitude, decay, shape etc., can be used as evidence for a relatively localized occurrence. Changes in the character of the EM responses, however, may be simply reflecting differences in the conductive formations themselves rather than indicating the presence of massive sulphides and, for this reason, the degree of confidence is reduced.

Another useful guide for identifying localized variations within formational conductors is to examine the magnetic data in map or image form. Further study of the magnetic data can reveal the presence of faults, contacts, and other features, which, in turn, help define areas of potential economic interest.

Finally, once ground investigations begin, it must be remembered that the continual comparison of ground knowledge to the airborne information is an essential step in maximizing the usefulness of the airborne EM data.

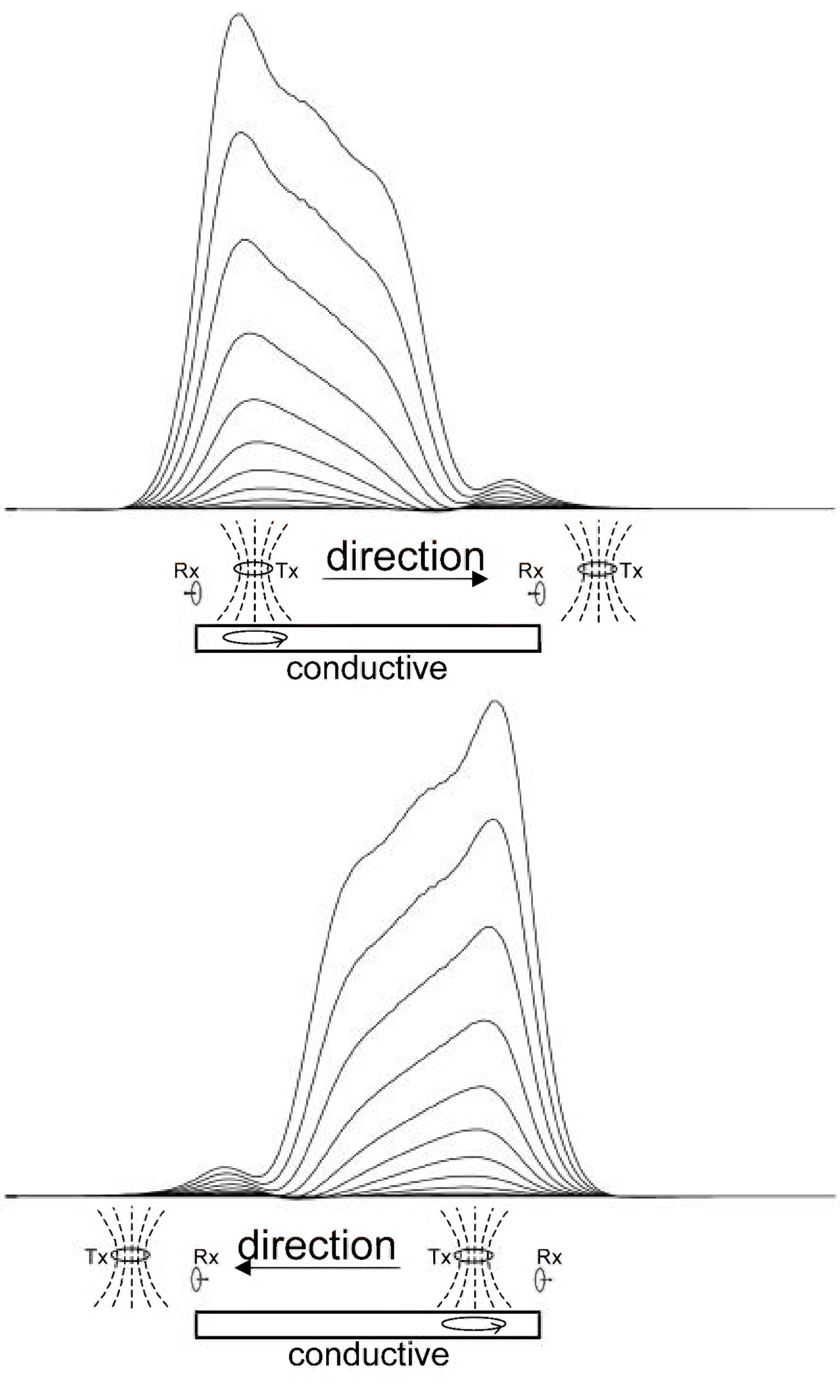

Figure 1. Illustration of how the x-component response varies depending on the flight direction. When the receiver flies onto the conductor, the transmitter is over the conductor and current is induced in the conductive material, resulting in a large response. When the receiver flies off the conductor, the transmitter is not over conductive material, so the response is small.

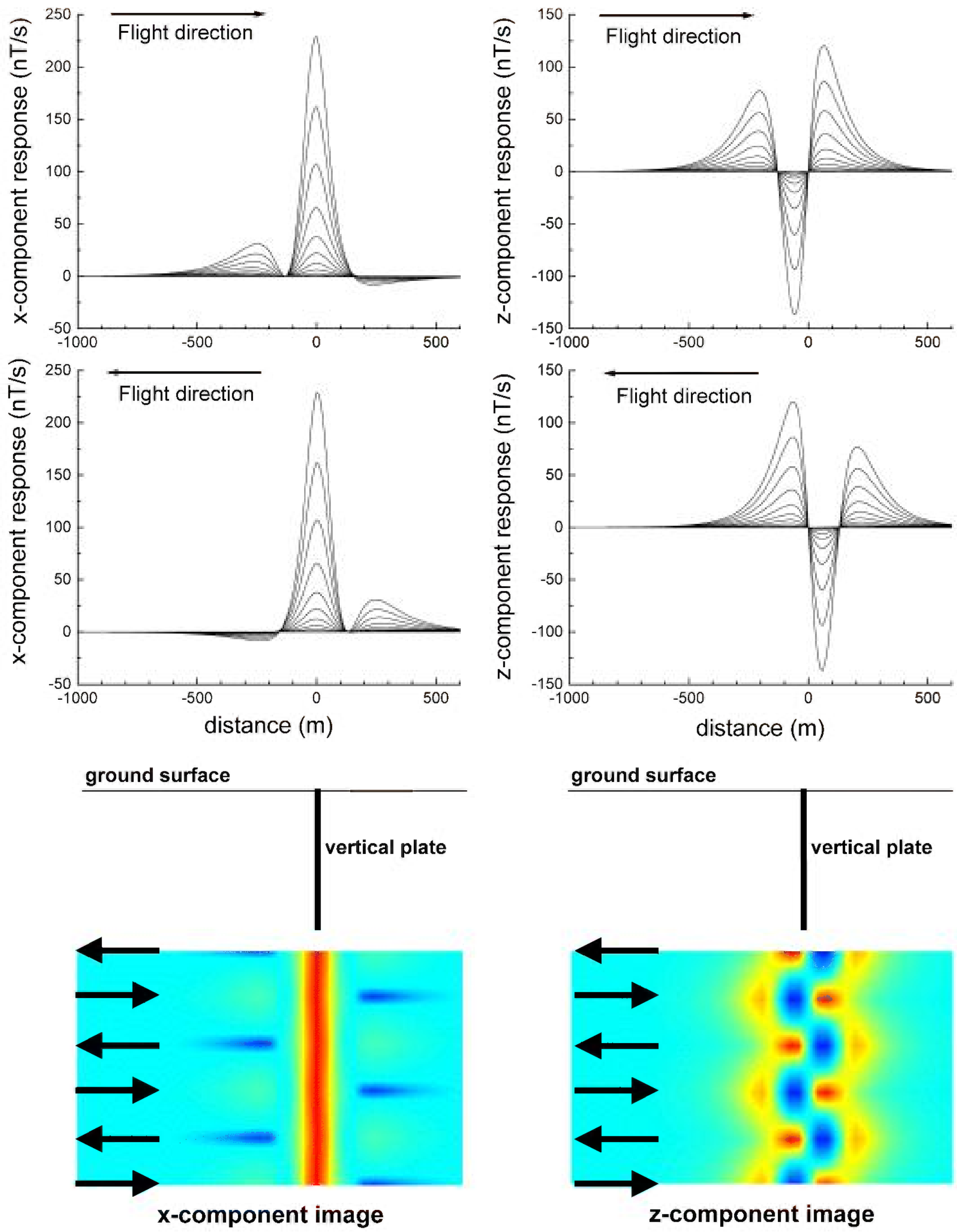

Figure 2. The response over a vertical plate. The left panels show the x-component, the right panels the z-component. The top is flying left to right, the middle is right to left, the bottom is a plan image with the alternating flight directions shown with arrows.

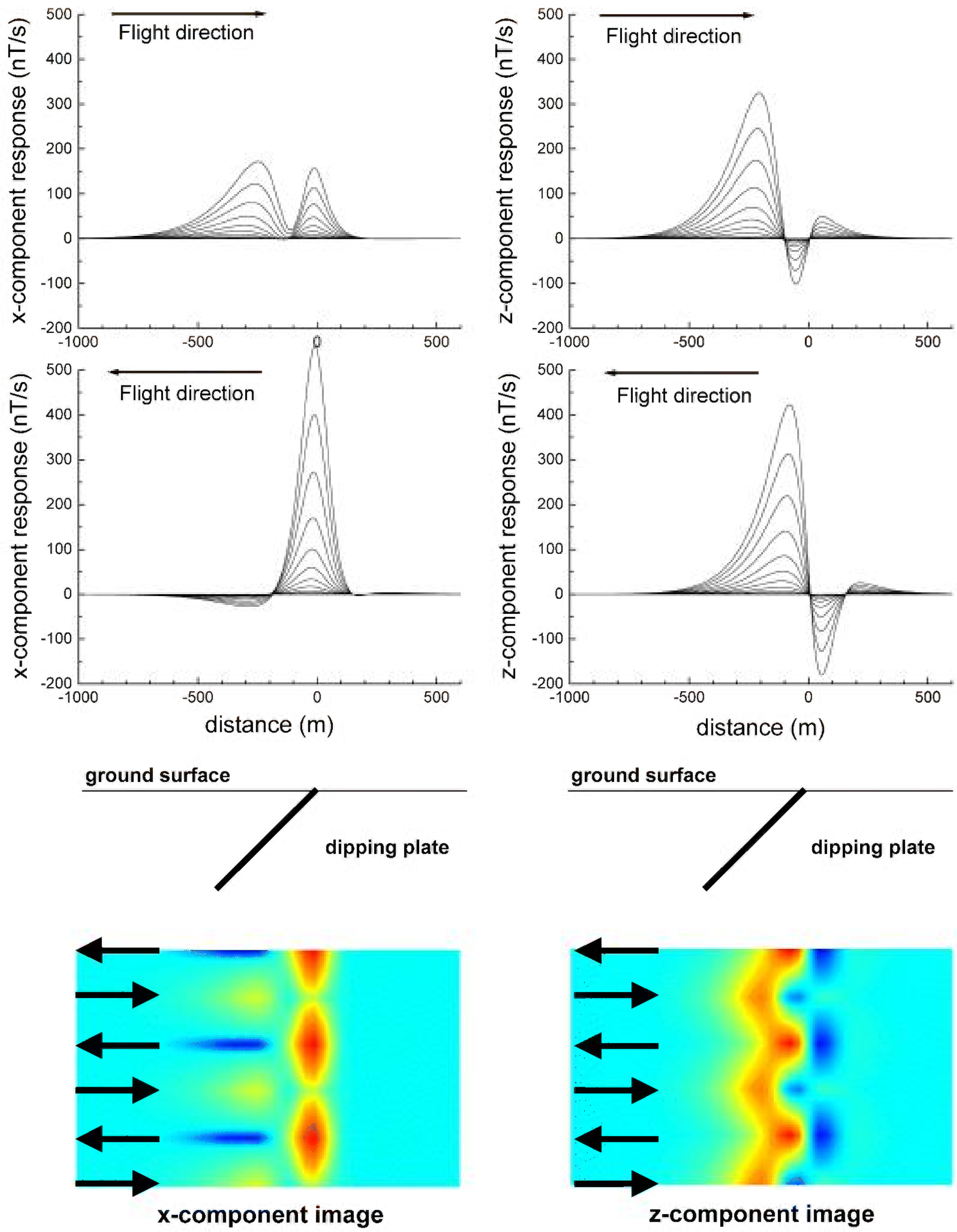

Figure 3. The response over a 45 degree dipping plate. The left panels show the x-component, the right panels the z-component. The top is flying left to right, the middle is right to left, the bottom is a plan image with the alternating flight directions shown with arrows.

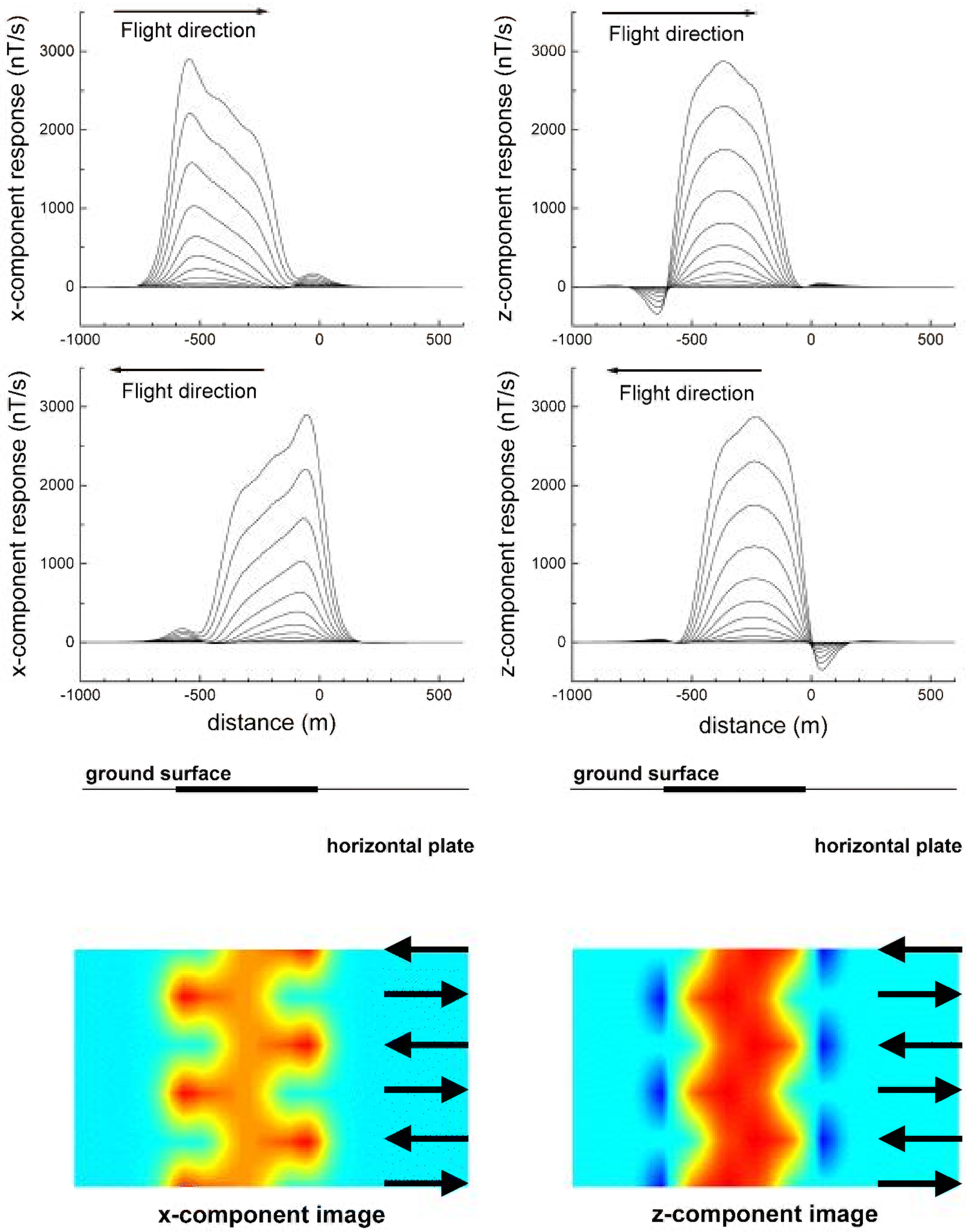

Figure 4. The response over a horizontal plate. The left panels show the x-component, the right panels the z-component. The top is flying left to right, the middle is right to left, the bottom is a plan image with the alternating flight directions shown with arrows.

Appendix C

Multi-component Modeling

Multi-component fixed-wing airborne EM modeling

PLATE MODELING

The PLATE program has been used to generate synthetic responses over a number of plate models with varying depth of burial (0, 150 and 300 m) and dips (0, 45, 90 and 135 degrees). The geometry assumed for the fixed-wing airborne EM system is shown on the following page (Figure 1), and the transmitter waveform on the subsequent page (Figure 2). In these models, the receiver is 130 m behind and 50 m below the transmitter center.

In all cases the plate has a strike length of 600 m, with a strike direction into the page. The width of the plate is 300 m. As the flight path traverses the center of the plate, the y-component is zero and has not been plotted.

The conductance of the plate is 20 S. In cases when the conductance is different, an indication of how the amplitudes may vary can be obtained from the nomogram included (Figure 3).

In the following profile plots (Figure 4 to 15) the plotting point is the receiver location and all of the component values are in nT/s, assuming a transmitter dipole moment of 900 000 Am^2. If the dipole moment is larger or smaller than 900 000 Am^2, then the response would be scaled up or down appropriately.

In the following profile plots (Figure 4 to 15) all components are in nT/s, for a transmitter dipole moment of 900 000 Am^2. If the dipole moment is larger or smaller, then the response should be scaled up or down appropriately.

The plotting point is the receiver location.

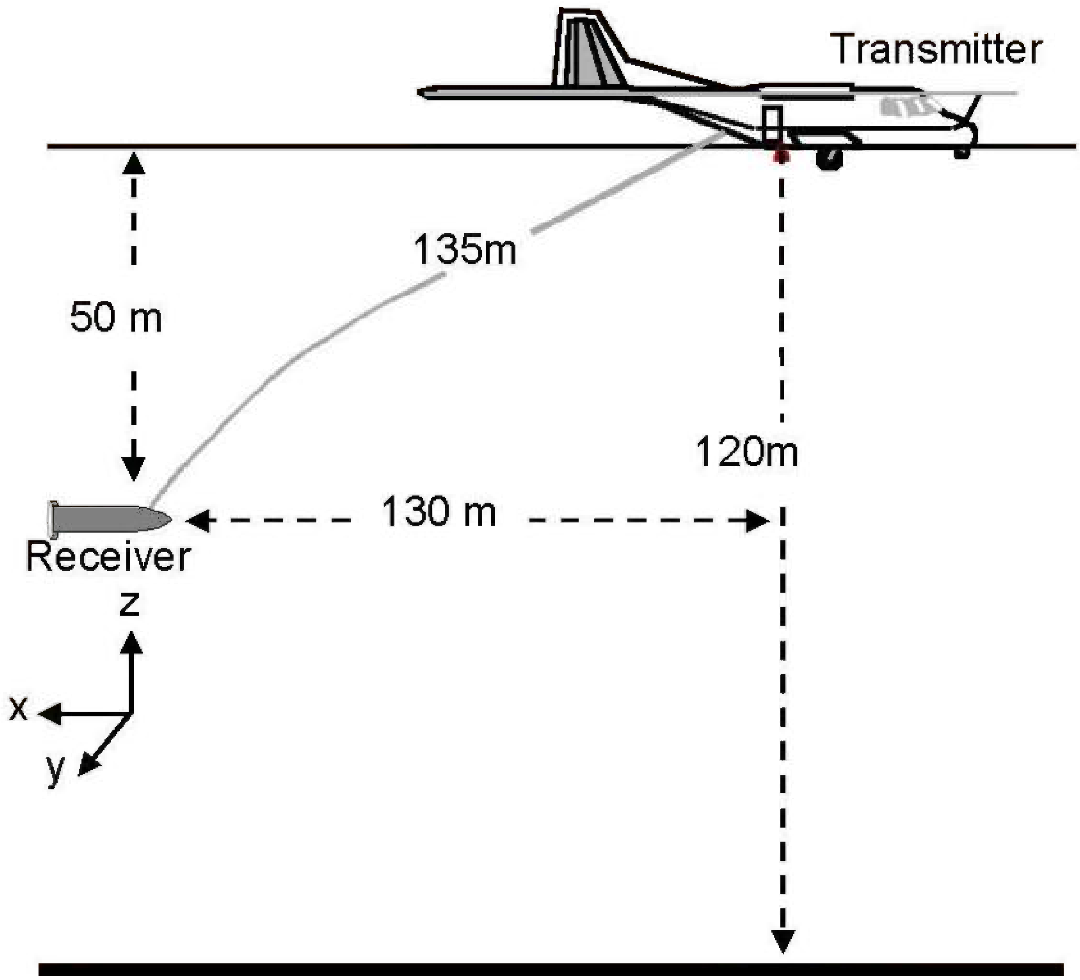

Figure 1. Nominal geometry of the MEGATEM® /GEOTEM® system.

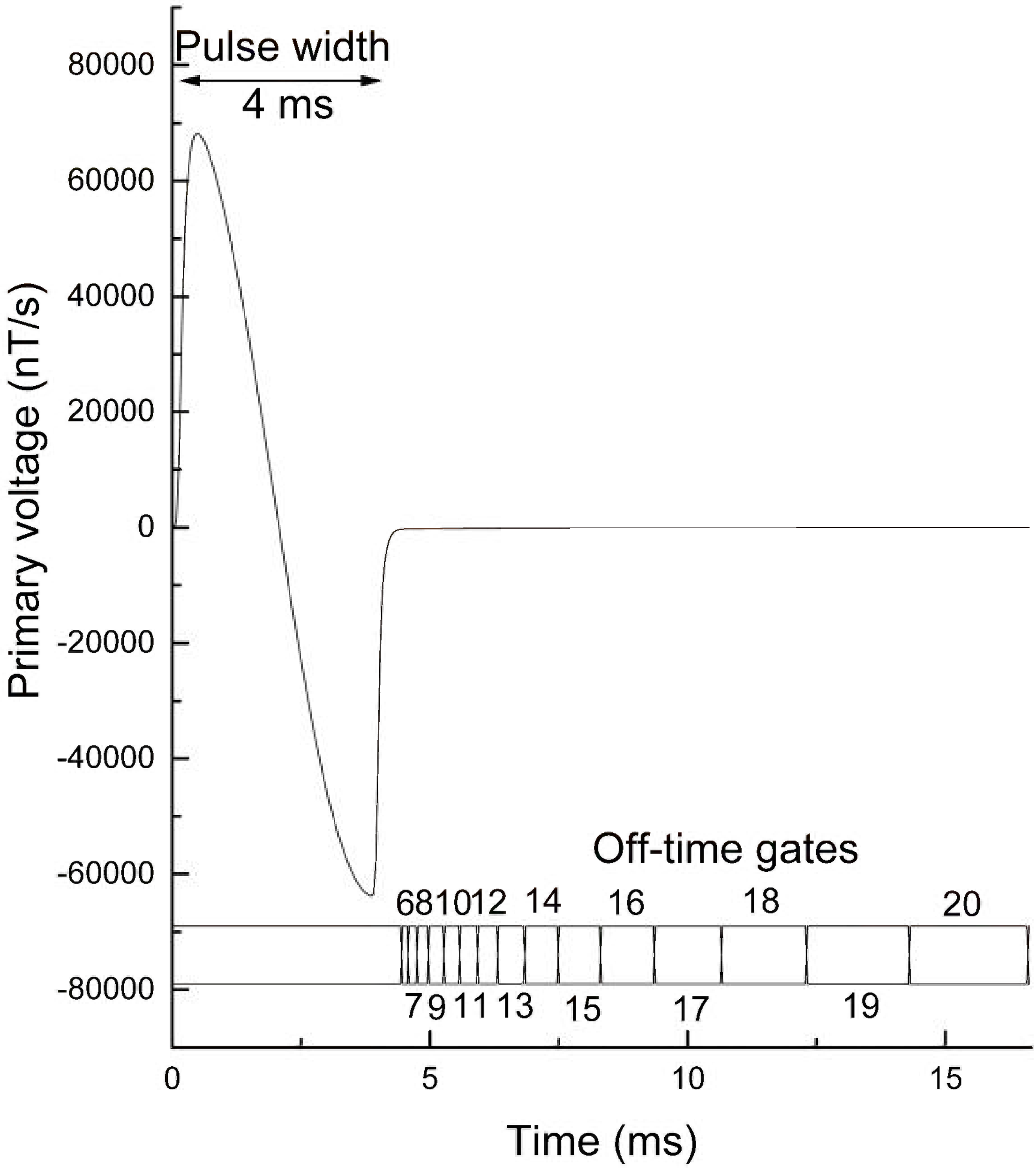

Figure 2. Theoretical transmitter waveform response in the receiver.

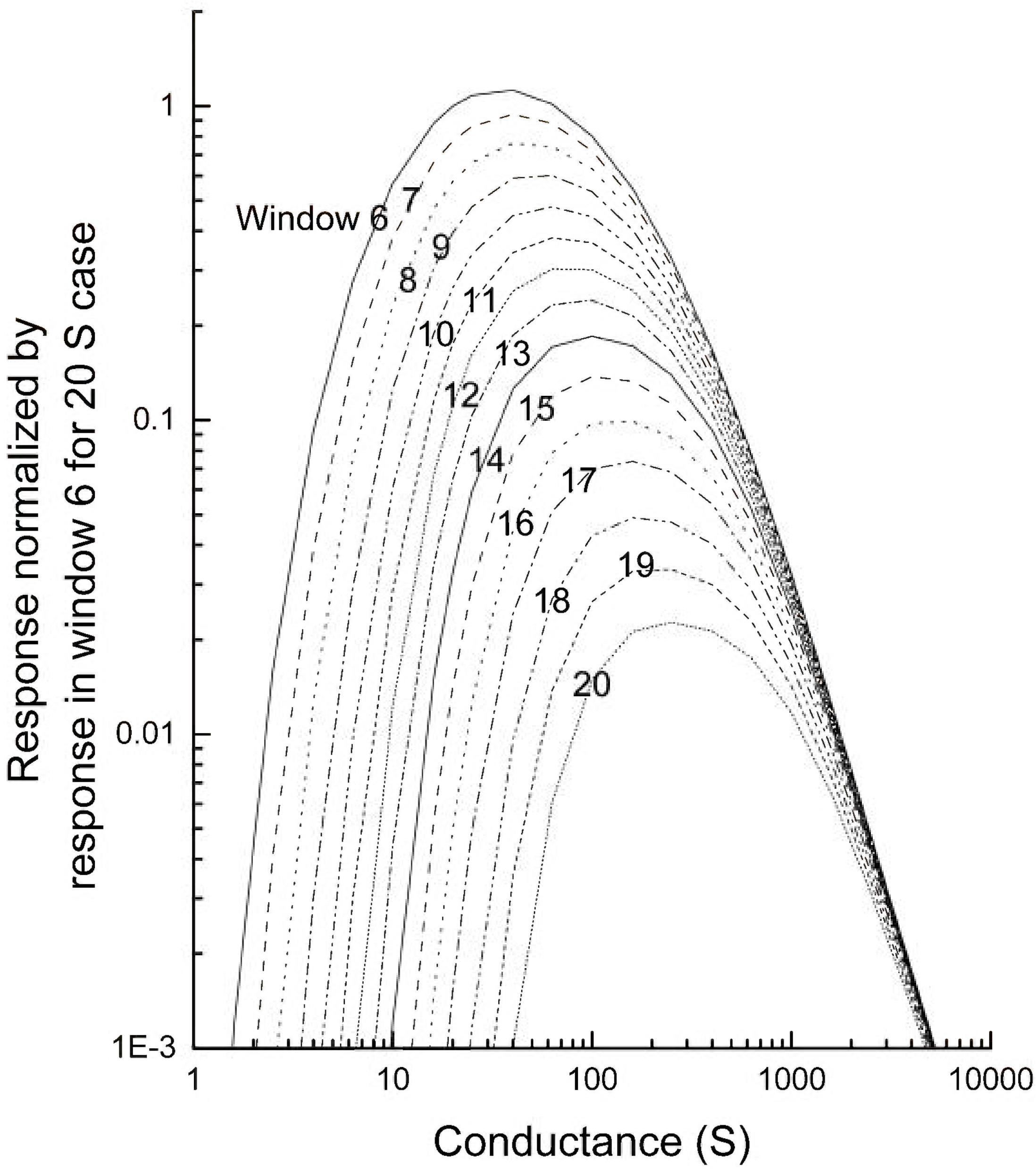

Figure 3. Nomogram for windows 6-20 normalized to a response from a 20-siemen conductor in window 6.

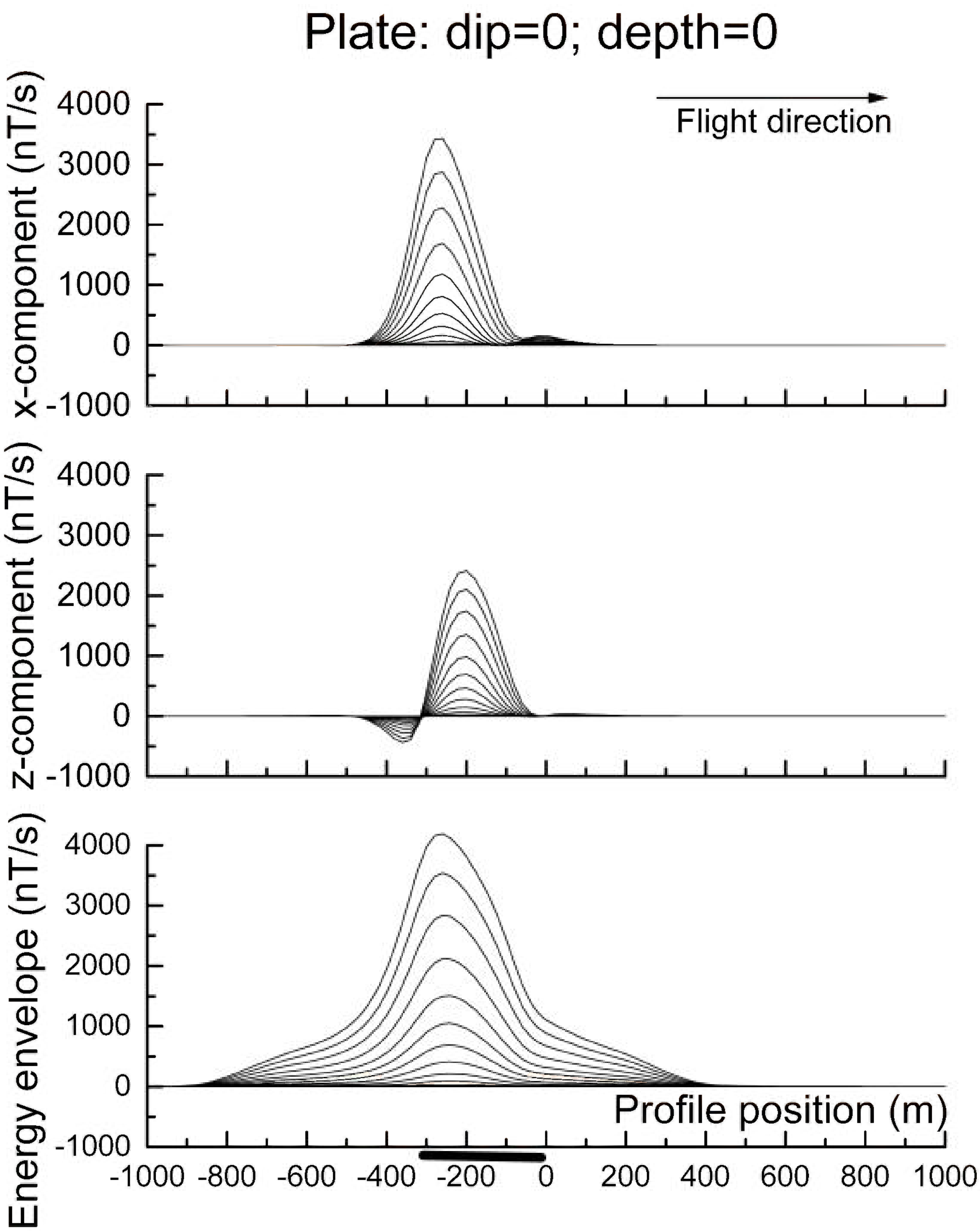
Plate: dip=0; depth=0
Flight direction
x-component (nT/s)
z-component (nT/s)
Energy envelope (nT/s)
Profile position (m)
4000
3000
2000
1000
0
-1000
-1000 -800 -600 -400 -200 0 200 400 600 800 1000

Figure 4.

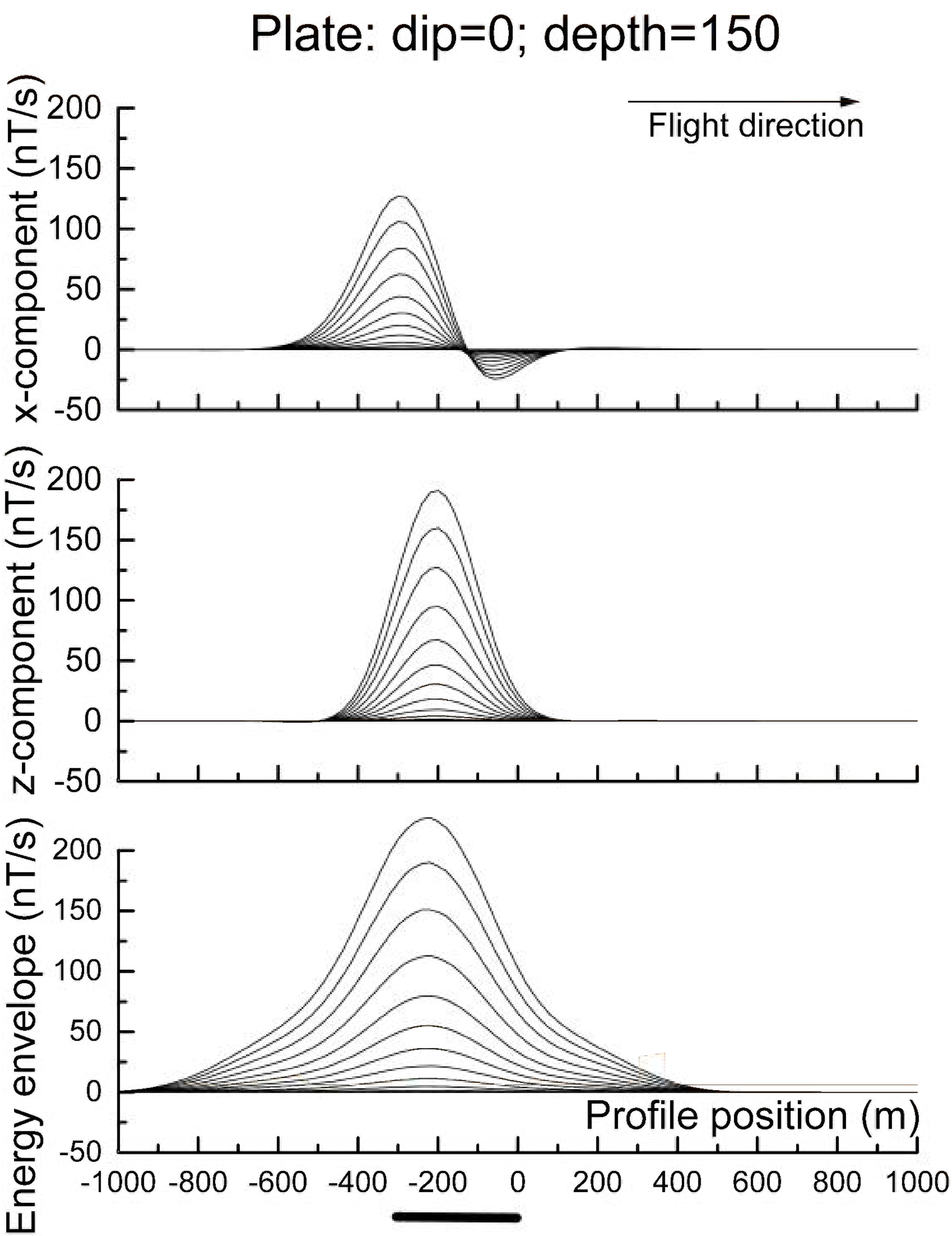
Plate: dip=0; depth=150
Flight direction
x-component (nT/s)
z-component (nT/s)
Energy envelope (nT/s)
Profile position (m)
200
150
100
50
0
-50
-1000 -800 -600 -400 -200 0 200 400 600 800 1000

Figure 5.

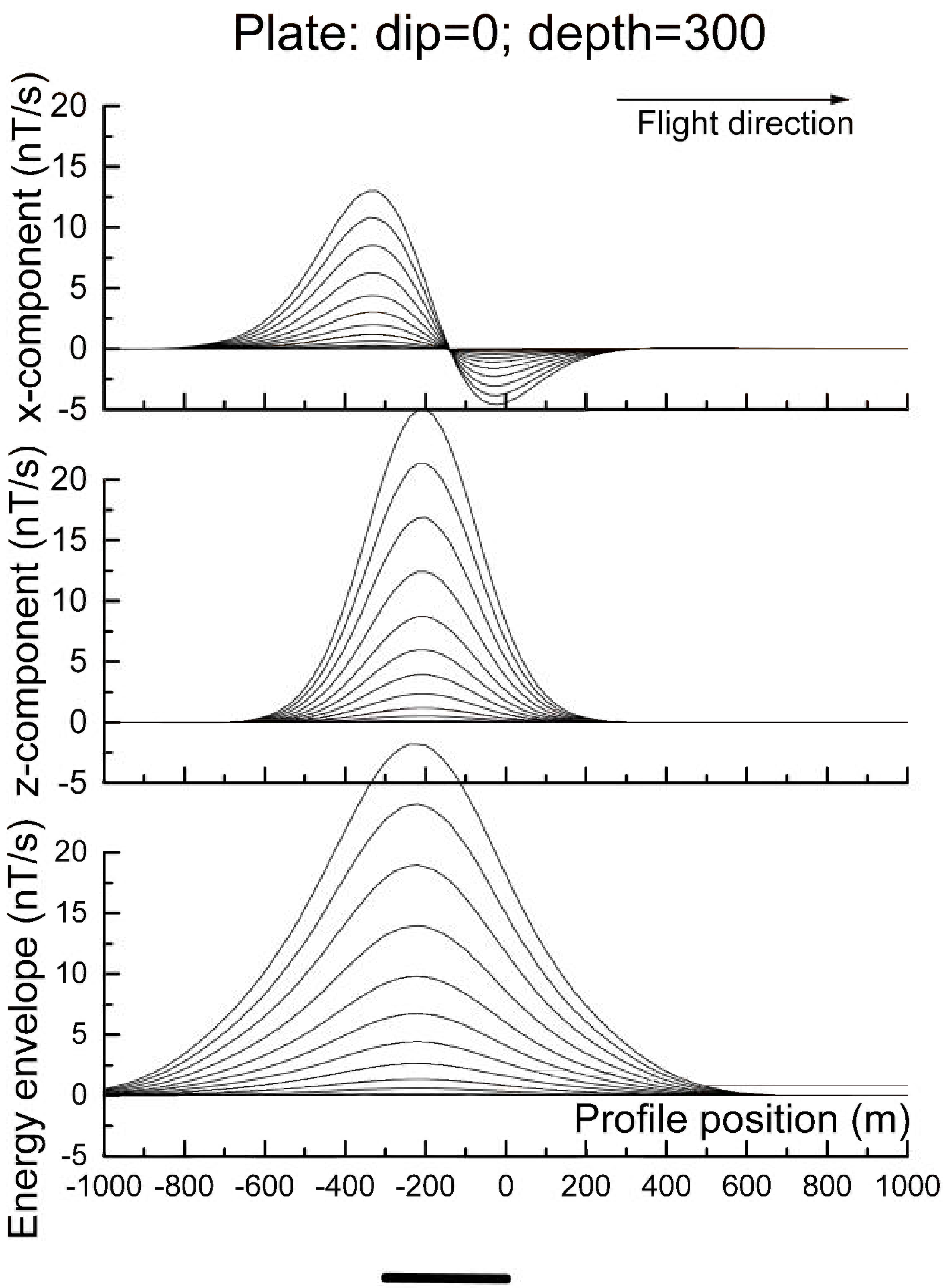

Plate: dip=0; depth=300
Flight direction
x-component (nT/s)
z-component (nT/s)
Energy envelope (nT/s)
Profile position (m)
20
15
10
5
0
-5
-1000 -800 -600 -400 -200 0 200 400 600 800 1000

Figure 6.

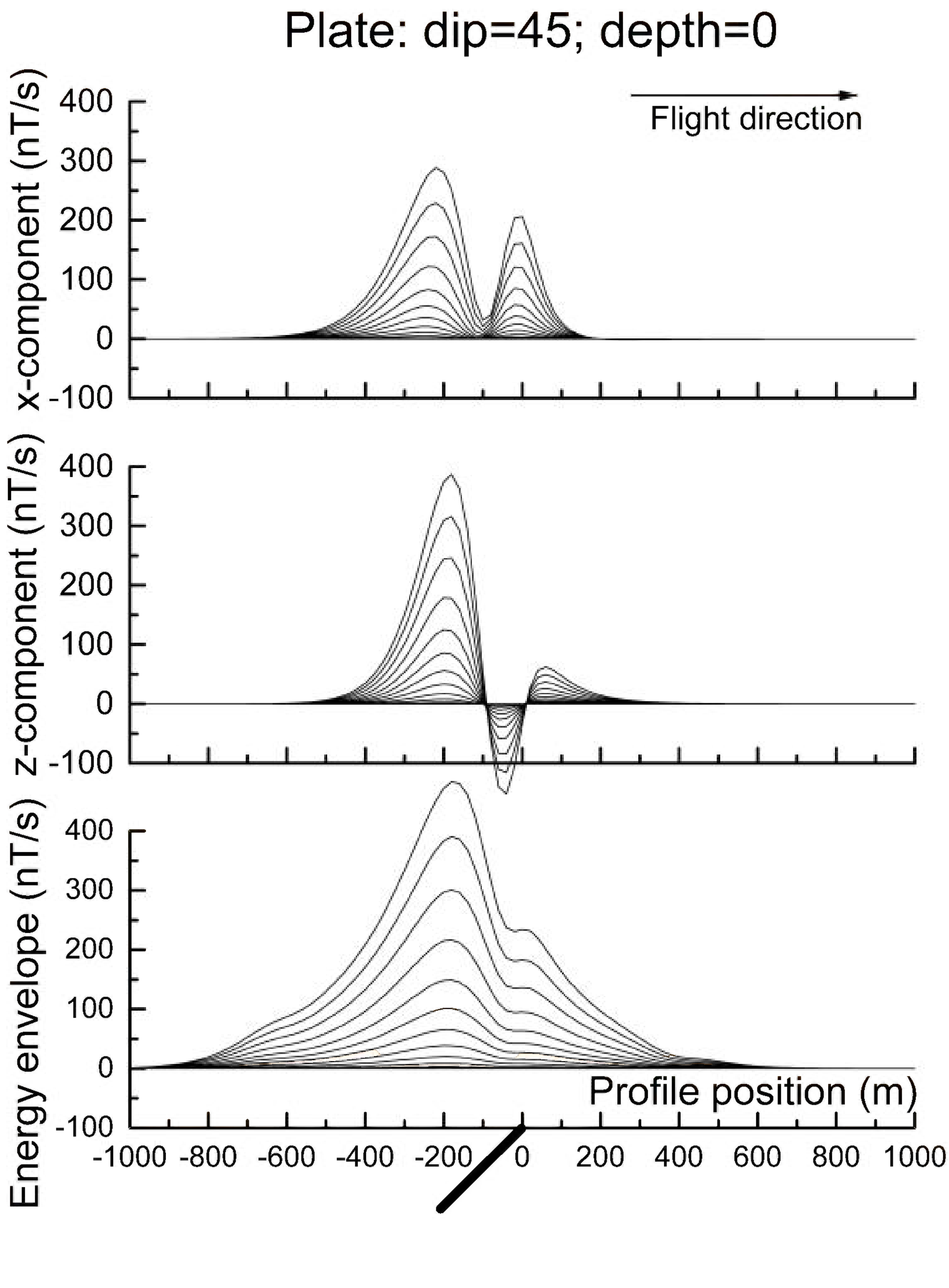

Plate: dip=45; depth=0
Flight direction
x-component (nT/s)
400
300
200
100
0
-100
z-component (nT/s)
400
300
200
100
0
-100
Energy envelope (nT/s)
400
300
200
100
0
-100
Profile position (m)
-1000 -800 -600 -400 -200 0 200 400 600 800 1000

Figure 7.

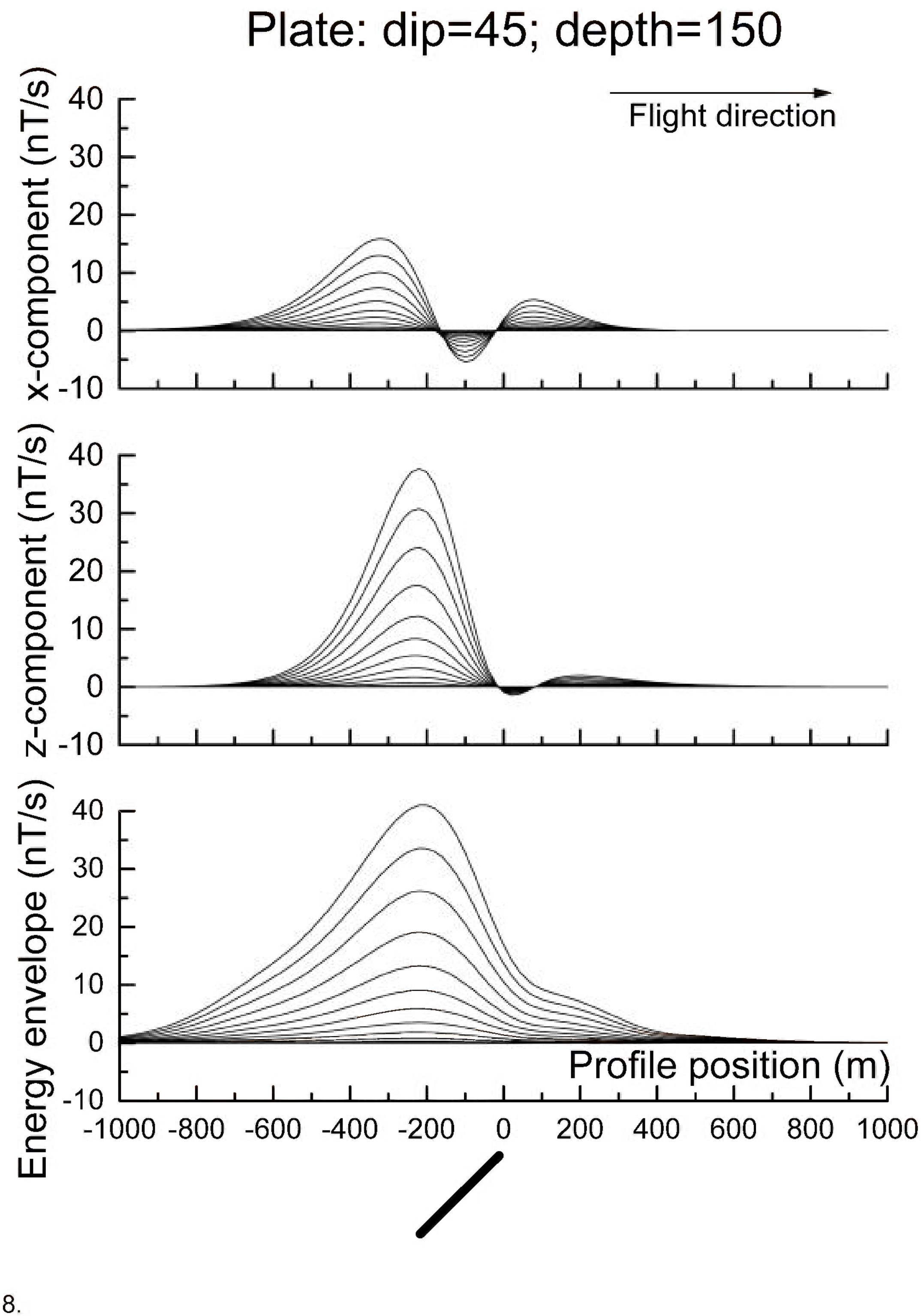
Plate: dip=45; depth=150
Flight direction
x-component (nT/s)
z-component (nT/s)
Energy envelope (nT/s)
Profile position (m)
40
30
20
10
0
-10
-1000
-800
-600
-400
-200
0
200
400
600
800
1000

Figure 8.

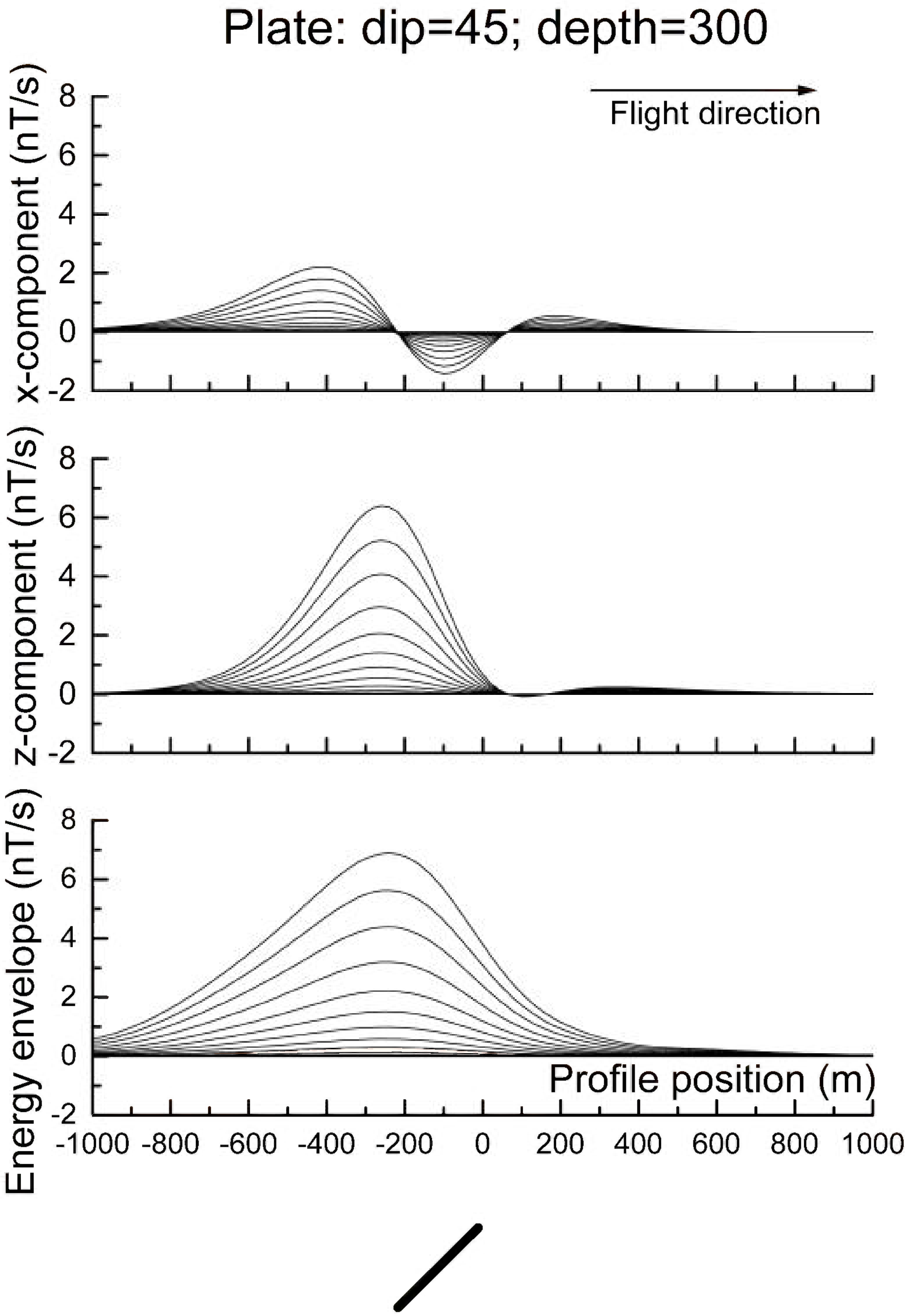
Plate: dip=45; depth=300
Flight direction
x-component (nT/s)
z-component (nT/s)
Energy envelope (nT/s)
Profile position (m)
8
6
4
2
0
-2
-1000 -800 -600 -400 -200 0 200 400 600 800 1000

Figure 9.

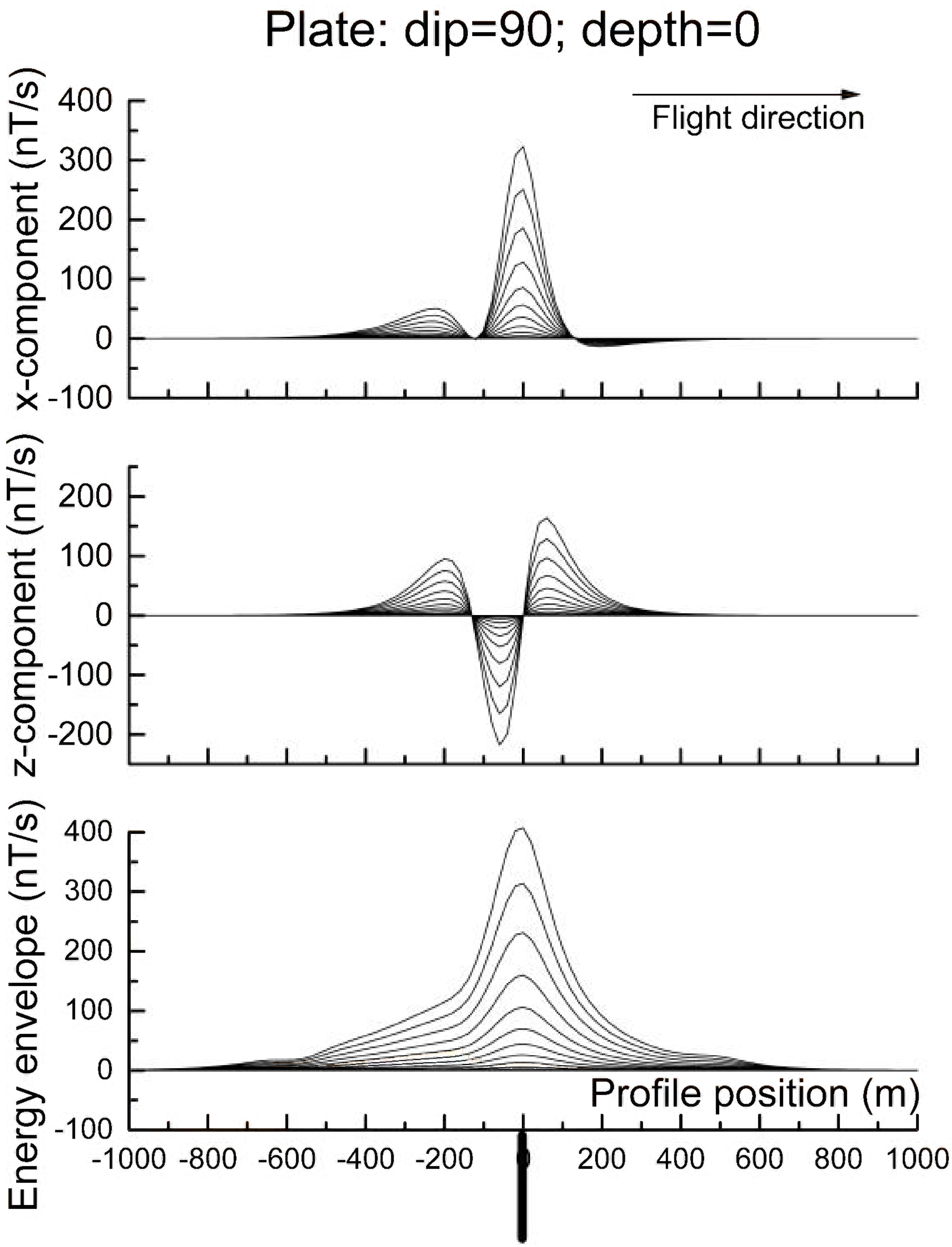
Plate: dip=90; depth=0
Flight direction
x-component (nT/s)
400
300
200
100
0
-100
z-component (nT/s)
200
100
0
-100
-200
Energy envelope (nT/s)
400
300
200
100
0
-100
Profile position (m)
-1000 -800 -600 -400 -200 0 200 400 600 800 1000

Figure 10.

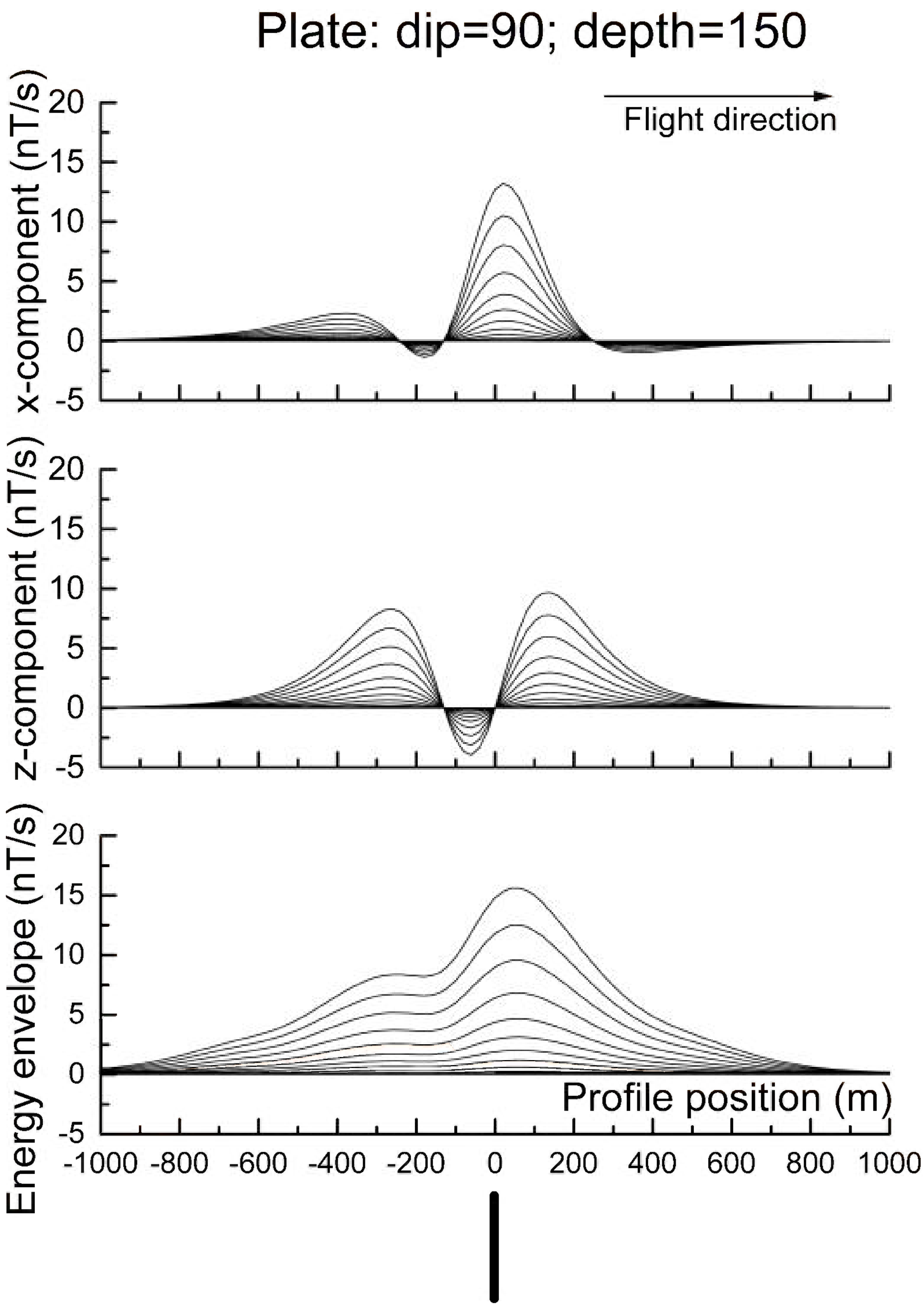
Plate: dip=90; depth=150
Flight direction
x-component (nT/s)
20
15
10
5
0
-5
z-component (nT/s)
20
15
10
5
0
-5
Energy envelope (nT/s)
20
15
10
5
0
-5
Profile position (m)
-1000 -800 -600 -400 -200 0 200 400 600 800 1000

Figure 11.

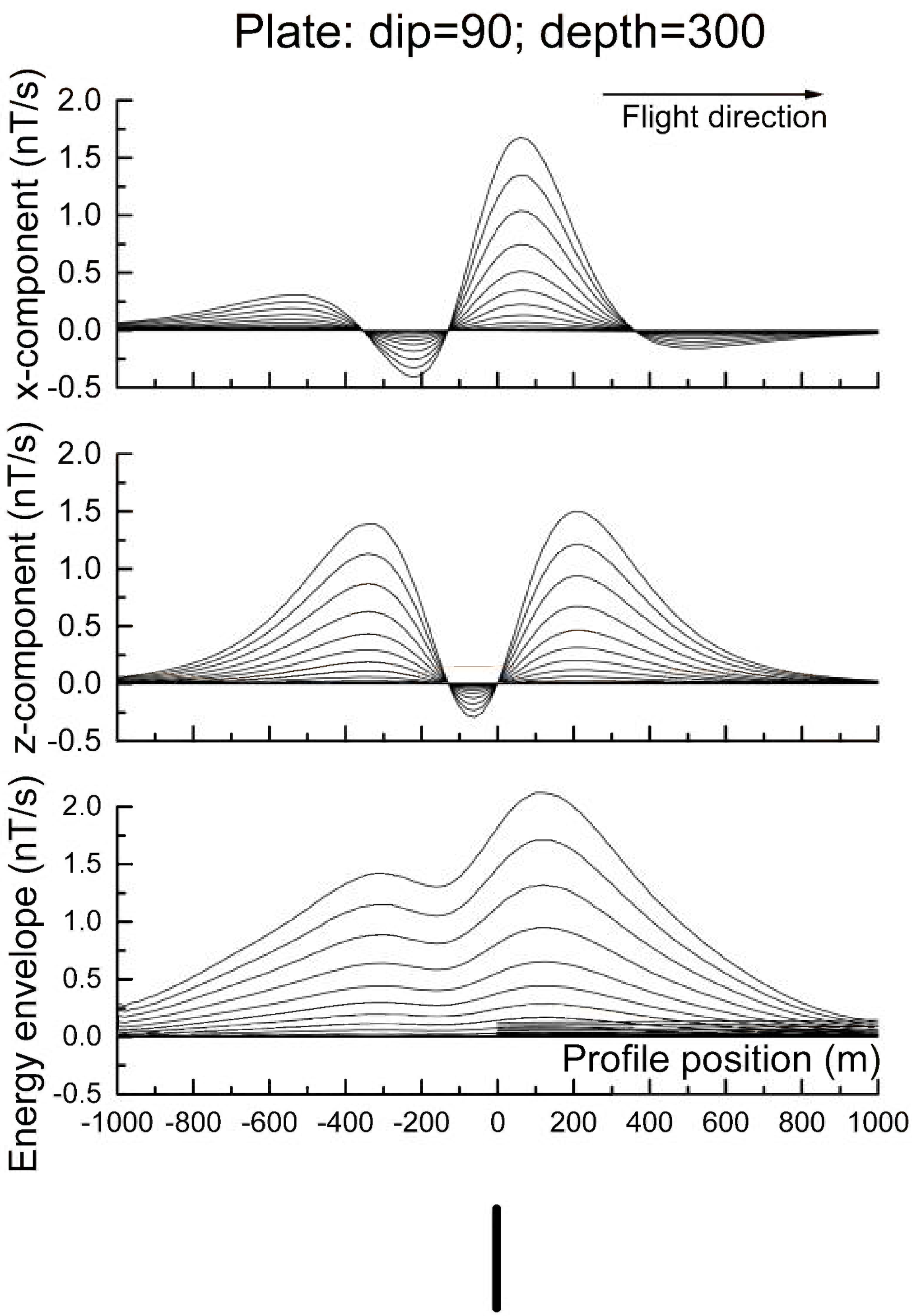
Plate: dip=90; depth=300
Flight direction
x-component (nT/s)
z-component (nT/s)
Energy envelope (nT/s)
Profile position (m)
2.0
1.5
1.0
0.5
0.0
-0.5
-1000 -800 -600 -400 -200 0 200 400 600 800 1000

Figure 12.

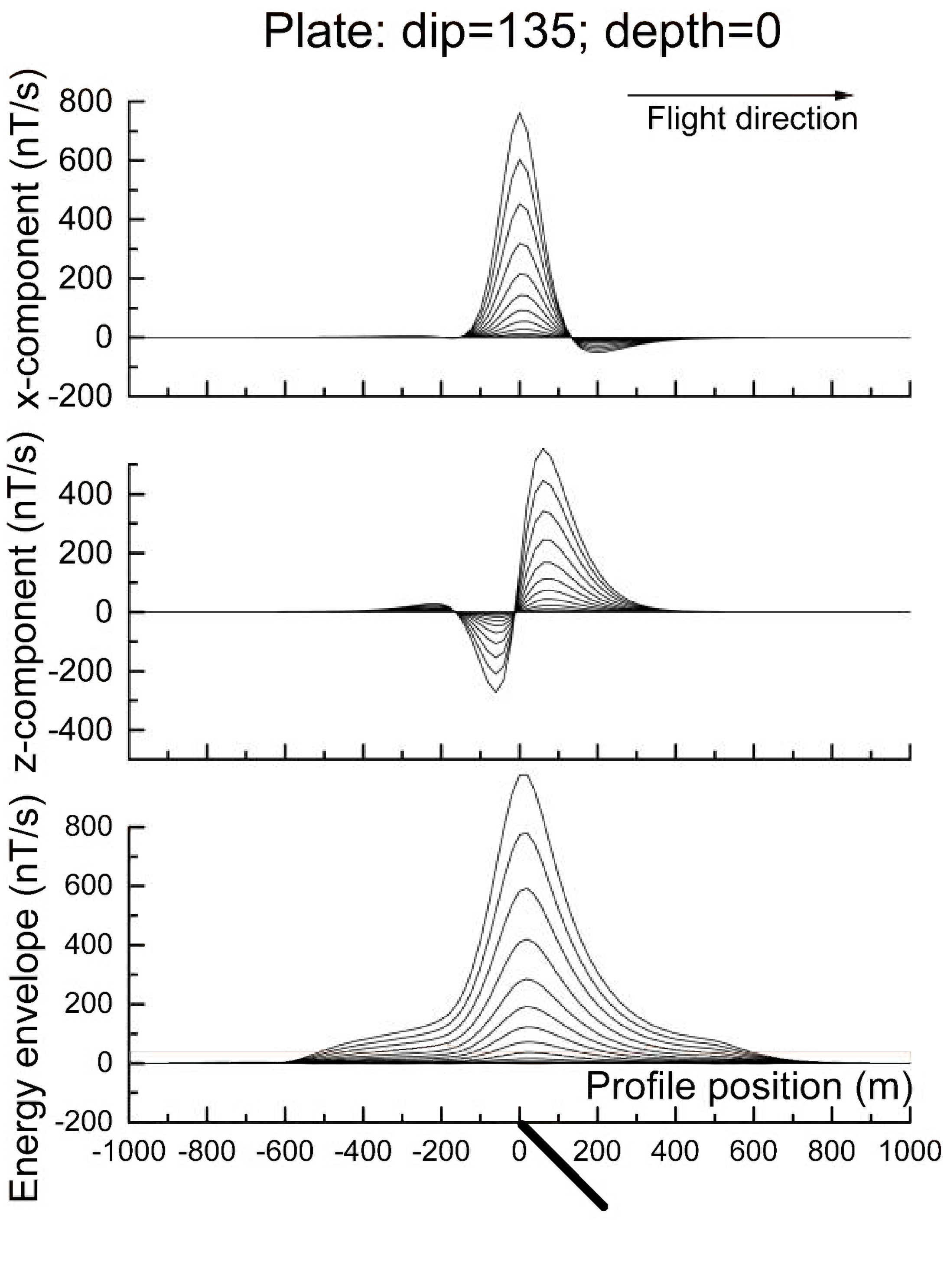

Plate: dip=135; depth=0
Flight direction
x-component (nT/s)
800
600
400
200
0
-200
z-component (nT/s)
400
200
0
-200
-400
Energy envelope (nT/s)
800
600
400
200
0
-200
Profile position (m)
-1000 -800 -600 -400 -200 0 200 400 600 800 1000

Figure 13.

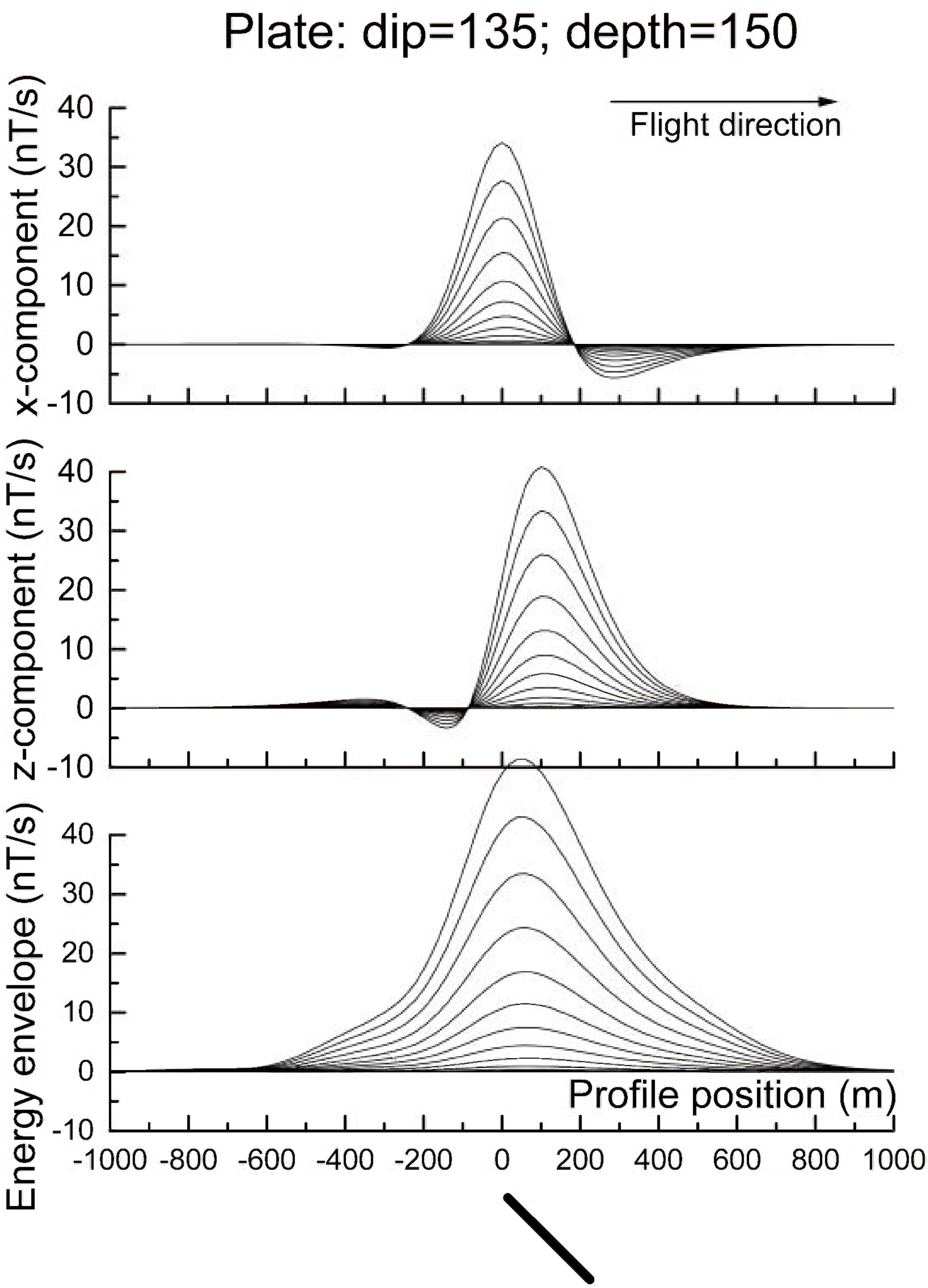
Plate: dip=135; depth=150
Flight direction
x-component (nT/s)
z-component (nT/s)
Energy envelope (nT/s)
Profile position (m)
40
30
20
10
0
-10
-1000 -800 -600 -400 -200 0 200 400 600 800 1000

Figure 14.

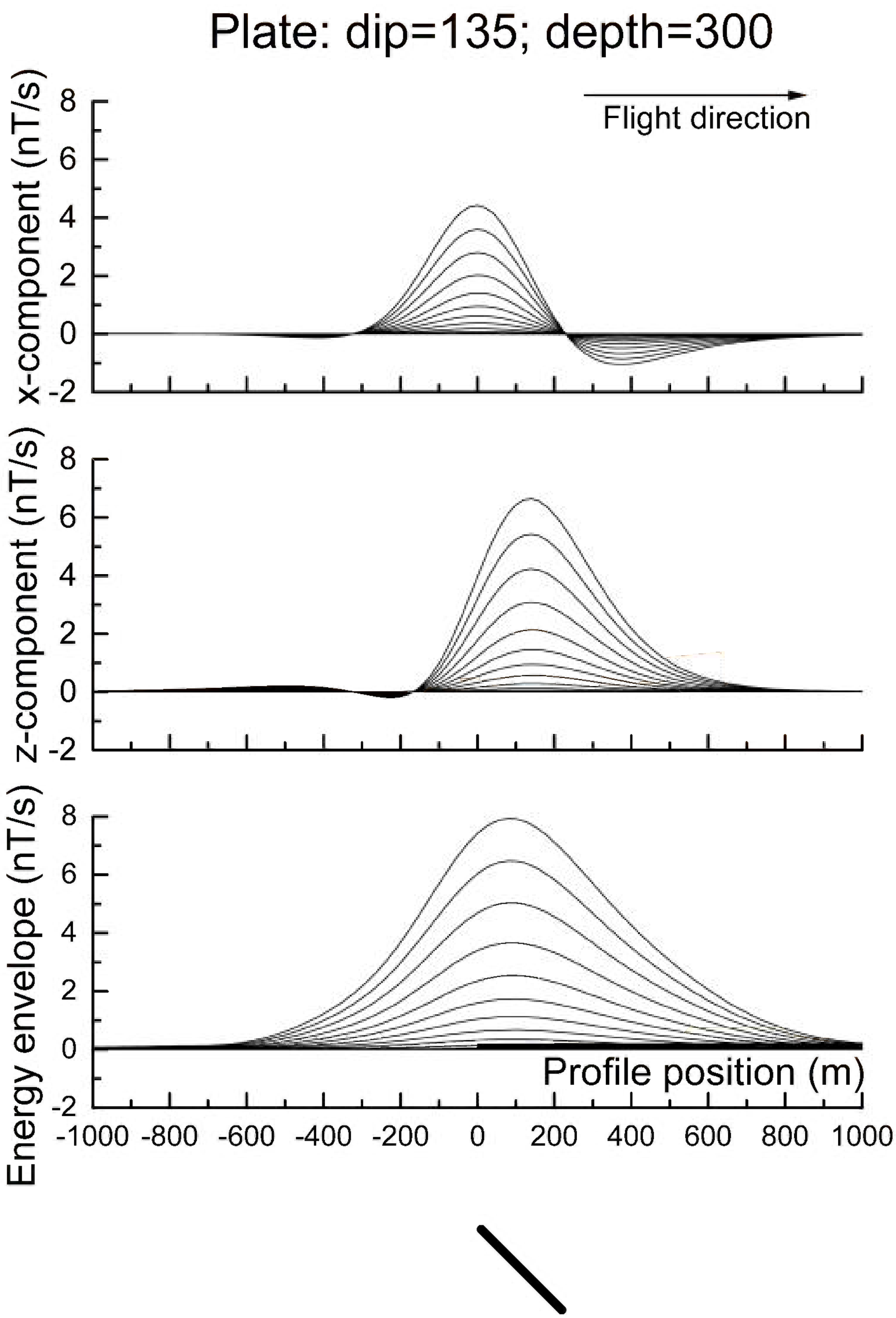
Plate: dip=135; depth=300
Flight direction
x-component (nT/s)
z-component (nT/s)
Energy envelope (nT/s)
Profile position (m)
8
6
4
2
0
-2
-1000 -800 -600 -400 -200 0 200 400 600 800 1000

Figure 15.

SPHERE MODELING

The sphere in a uniform field program (Smith and Lee, Exploration Geophysics, 2001, pp 113-118) has been used to generate synthetic responses over a number of sphere models with varying depth of burial (0, 150 and 300 m). The geometry assumed for the fixed-wing airborne EM system and the waveform are as shown in Figures 1 and 2 above.

In all cases the sphere has a radius of 112 m. As the flight path traverses the center of the sphere, the y component is zero and has not been plotted.

The conductivity of the sphere is 1 S/m. In cases when the conductivity is different, an indication of how the amplitudes may vary can be obtained from the nomogram that follows (Figure 16).

In the following profile plots (Figure 17 to 19) all components are in nT/s, for a transmitter dipole moment of 900 000 Am^2. If the dipole moment is larger or smaller, then the response should be scaled up or down appropriately.

The plotting point is the receiver location.

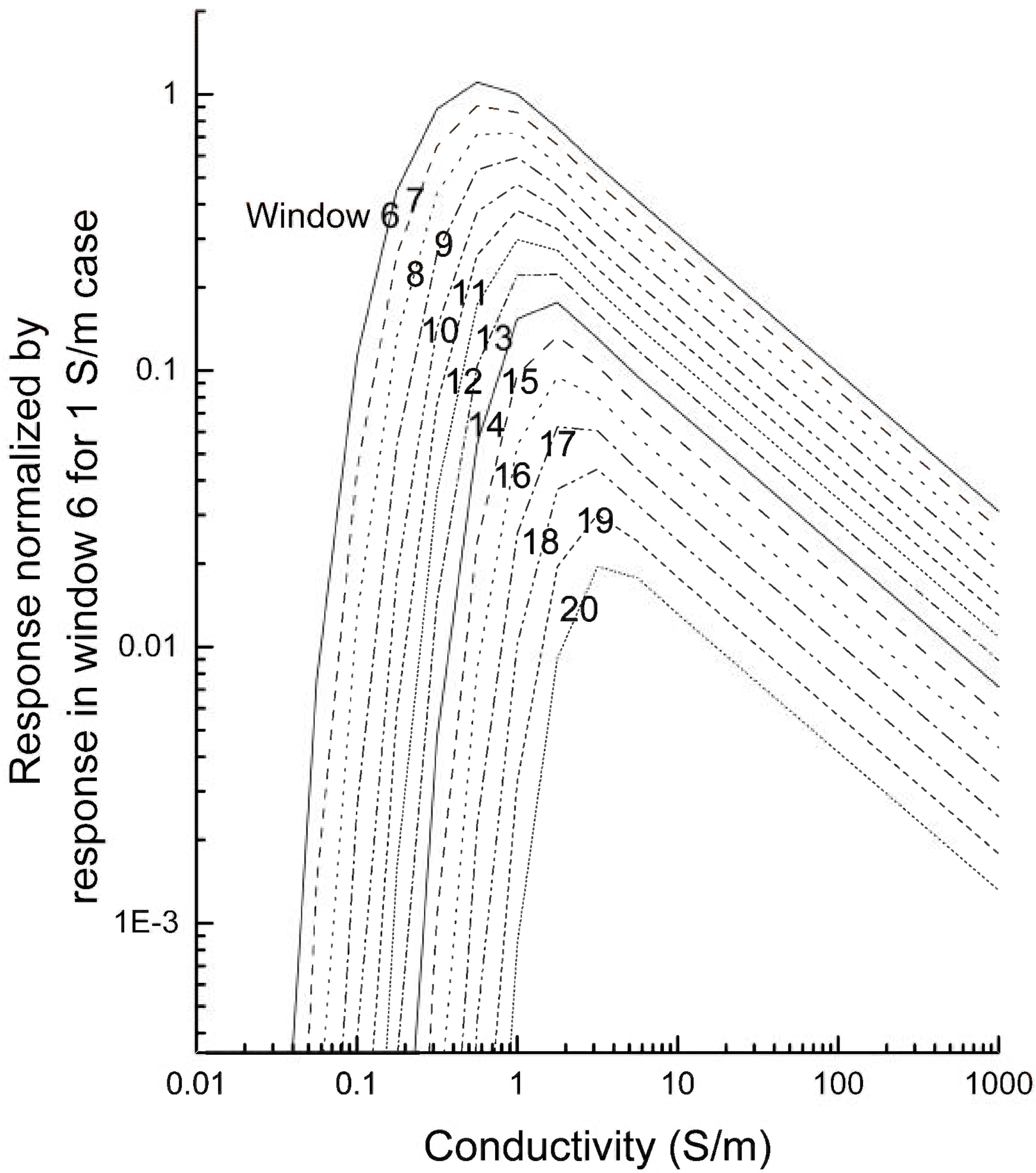

Figure 16. Nomogram for windows 6-20 normalized to a response from a 1-siemen conductor in window 6.

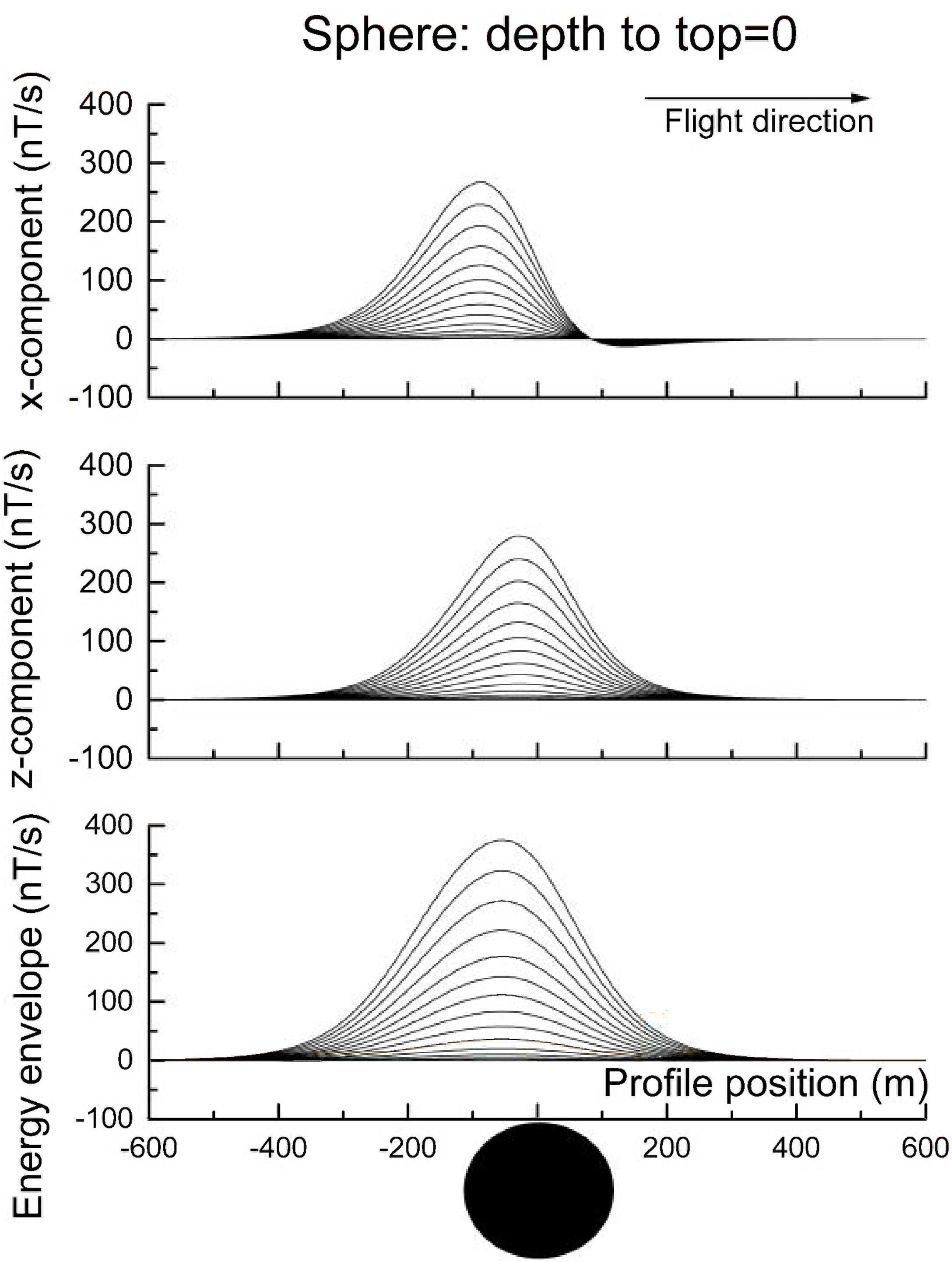

Sphere: depth to top=0
Flight direction
x-component (nT/s)
400
300
200
100
0
-100
z-component (nT/s)
400
300
200
100
0
-100
Energy envelope (nT/s)
400
300
200
100
0
-100
Profile position (m)
-600
-400
-200
200
400
600

Figure 17.

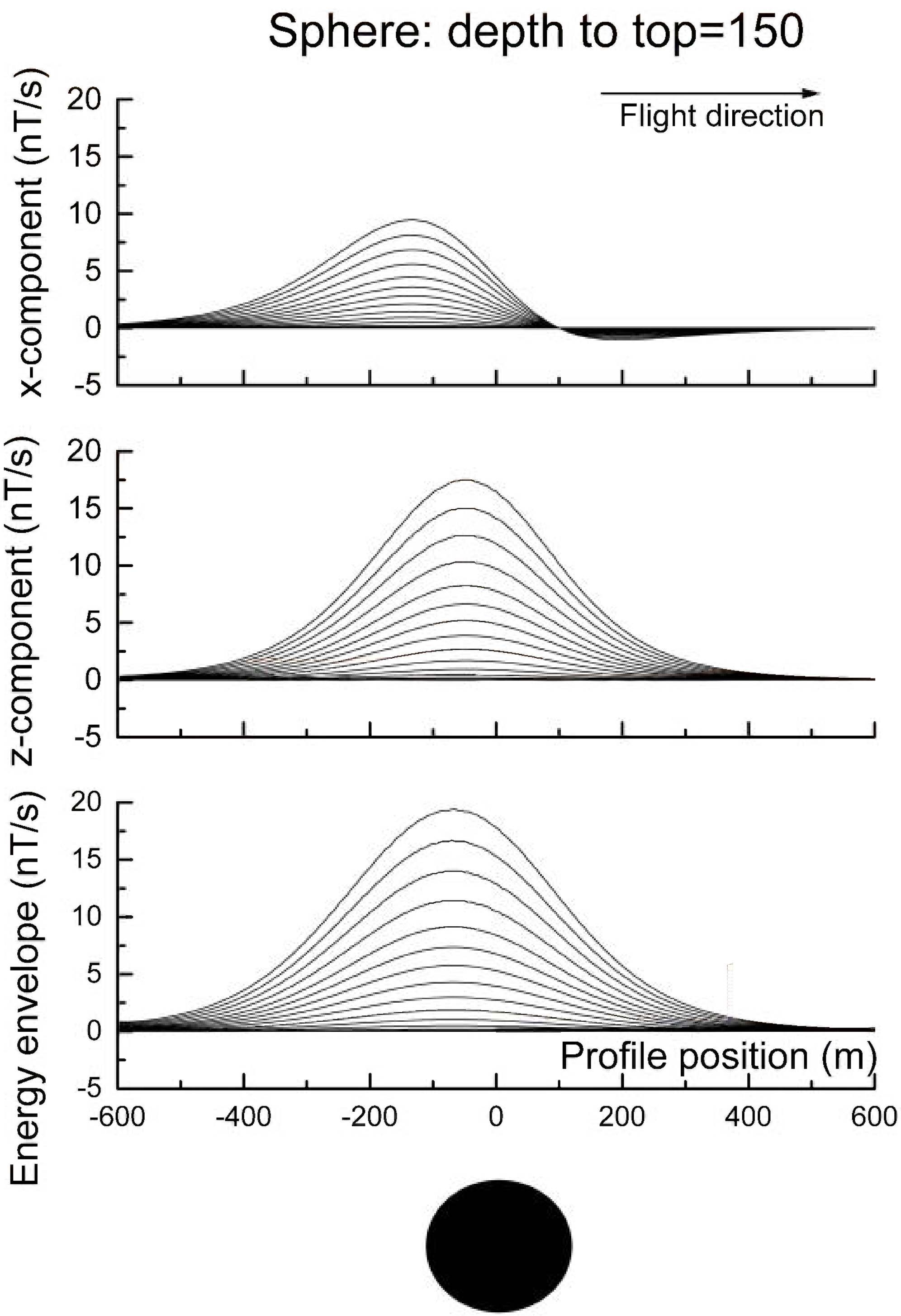

Sphere: depth to top=150
Flight direction
x-component (nT/s)
z-component (nT/s)
Energy envelope (nT/s)
Profile position (m)
20
15
10
5
0
-5
-600
-400
-200
0
200
400
600

Figure 18.

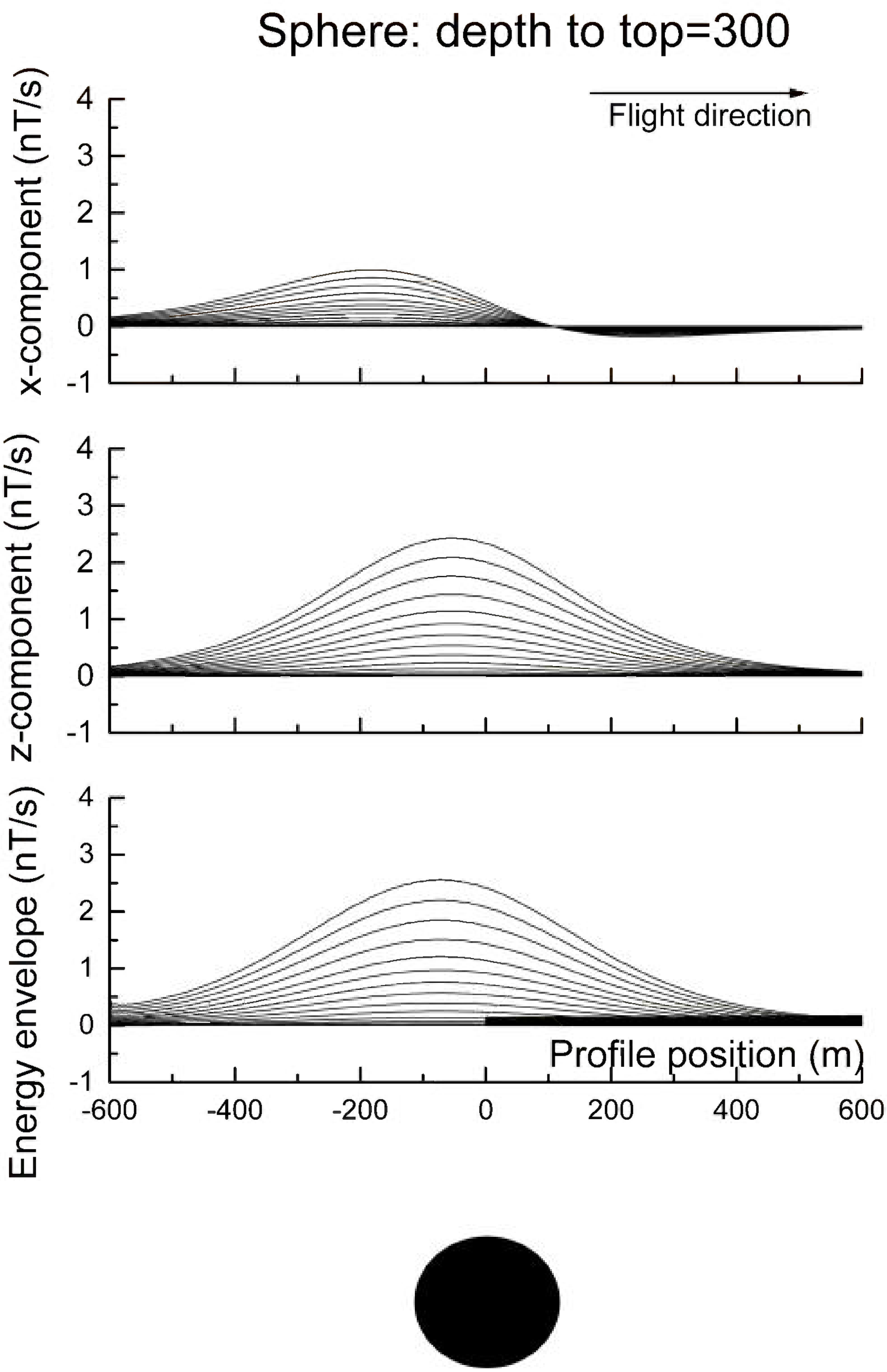

Sphere: depth to top=300
Flight direction
x-component (nT/s)
z-component (nT/s)
Energy envelope (nT/s)
Profile position (m)
4
3
2
1
0
-1
-600
-400
-200
0
200
400
600

Figure 19.

Appendix D

The Usefulness of Multi-component, Time-Domain Airborne Electromagnetic Measurement

GEOPHYSICS, VOL 61, NO. 1 (JANUARY-FEBRUARY 1996); P. 74-81, 17 FIGS.

The usefulness of multi-component, time-domain airborne electromagnetic measurements

Richard S. Smith* and Pierre B. Keating ‡

ABSTRACT

Time-domain airborne electromagnetic (AEM) systems historically measure the inline horizontal (*x*) component. New versions of the electromagnetic systems are designed to collect two additional components [the vertical (*z*) and the lateral horizontal (*y*) component] to provide greater diagnostic information.

In areas where the geology is near horizontal, the *z* component response provides greater signal to noise, particularly at late delay times. This allows the conductivity to be determined to greater depth. In a layered environment, the symmetry implies that the *y* component will be zero; hence a non-zero *y* component will indicate a lateral inhomogeneity.

The three components can be combined to give the "energy envelope" of the response. Over a vertical plate, the response profile of this envelope has a single positive peak and no side lobes. The shape of the energy envelope is dependent on the flight direction, but less so than the shape of the *x* component response profile.

In the interpretation of discrete conductors, the *z* component data can be used to ascertain the dip and depth to the conductor using simple rules of thumb. When the profile line is perpendicular to the strike direction and over the center of the conductor, the *y* component will be zero; otherwise it appears to be a combination of the *x* and *z* components. The extent of the contamination of the y component by the *x* and *z* components can be used to ascertain the strike direction and the lateral offset of the target, respectively.

Having the *z* and *y* component data increases the total response when the profile line has not traversed the target. This increases the possibility of detecting a target located between adjacent flight lines or beyond a survey boundary.

Presented at the Airborne Electromagnetics Workshop, Tucson, AZ, September 13-16, 1993. Manuscript received by the Editor February 28, 1994; revised manuscript received September 16, 1994.
*Geoterrex, 2060 Walkley Rd., Ottawa, Ontario, K1G 3P5, Canada.
‡Geological Survey of Canada, 1 Observatory Crescent, Ottawa, Ontario K1A 0Y3, Canada.

INTRODUCTION

The acquisition of multiple-component electromagnetic (EM) data is becoming more commonplace. In some techniques, such as those which use the plane-wave assumption (MT, CSAMT and VLF) more than one component has been acquired as a matter of routine for some time (see reviews by Vozoff, 1990, 1991; Zonge and Hughes, 1991; McNeill and Labson, 1991). Historically, commercially available controlled-waveform finite-source systems generally measure only one component. The only systems designed to acquire multiple component data are generally experimental [e.g., those described in the appendixes of Spies and Frischknecht (1991) or proprietary (the EMP system of Newmont Exploration).

Slingram EM systems, comprising a moving dipolar transmitter and a moving receiver, generally only measure one component of the response. Although the MaxMin system was designed with a capability to measure a second (minimum coupled) component, this capability is not used extensively in practice. The only systems that use two receiver coils in practice are those that measure the wavetilt or polarization ellipse (Frischknecht et al., 1991).

Historically, time-domain EM systems have been capable of collecting multi-component data in a sequential manner by reorienting the sensor for each component direction. The usefulness of additional components is discussed by Macnae (1984) for the case of the UTEM system. Macnae concluded that, as extra time was required to acquire the additional components, this time was better spent collecting more densely spaced vertical-component data. The vertical-component, which is less subject to spheric noise, could subsequently be converted to the horizontal components using the Hilbert transform operators.

Recent instrument developments have been towards multi-component systems. For example, commercially available ground-EM systems such as the Geonics PROTEM, the Zonge GDP-32 and the SIROTEM have been expanded to include multiple input channels that allow three (or more) components to be acquired simultaneously. There is also a version of the UTEM system currently being developed at Lamontagne Geophysics Ltd. These multichannel receivers require complimentary multi-component sensors -- for ground-based systems these have been developed by Geonics Ltd and Zonge Engineering and Research Organization. The interpretation of fixed-source, multi-component ground-EM data is described in Barnett (1984) and Macnae (1984).

In the past, multi-component borehole measurements have been hindered by the lack of availability of multi-component sensor probes. Following the development of two prototype probes (Lee, 1986; Hodges et al., 1991), multi-component sensors are now available from Crone Geophysics and Exploration Ltd and Geonics. Three component UTEM and SIROTEM borehole sensors are also in development at Lamontagne and Monash University (Cull, 1993), respectively. Hodges et al. (1991) present an excellent discussion of techniques that can be used to interpret three-component borehole data.

Airborne systems such as frequency-domain helicopter electromagnetic methods acquire data using multiple sensors. However, each receiver has a corresponding transmitter that either operates at a different frequency or has a different coil orientation (Palacky and West, 1991). Hence, these systems are essentially multiple single-component systems. The exception to this rule is the now superseded Dighem III system (Fraser, 1972) which used one transmitter and three receivers.

The only multi-component airborne EM (AEM) system currently in operation is the SPECTREM system (Macnae, et al., 1991). This is a proprietary system (owned and operated by

Anglo-American Corporation of South Africa Ltd.), based on the PROSPECT system (Annan, 1986). The Prospect system was originally designed to acquire the *x*, *y* and *z* components, but SPECTREM is apparently only collecting two components (x and z) at the time of writing. Other multi-component systems currently in development are:

1) the SALTMAP system,
2) a helicopter time-domain system (Hogg, 1986), and
3) a new version of the GEOTEM® system (GEOTEM is a registered trademark of Geoterrex).

Apart from a few type curves in Hogg (1986), there is little literature available which describes how to interpret data from these systems.

This paper is intended to give an insight into the types of responses expected with the new multi-component AEM systems, and the information that can be extracted from the data. The insight could be of some assistance in interpreting data from multi-component moving-source ground EM systems (should this type of data be acquired).

The use of multi-component data will be discussed for a number of different applications. For illustration purposes, this paper will use the transmitter-receiver geometry of the GEOTEM® system (Figure 1), which is comparable to the other fixed-wing geometries (SPECTREM and SALTMAP). The GEOTEM® system is a digital transient EM system utilizing a bipolar half-sinusoidal current waveform [for more details refer to Annan and Lockwood (1991)]. The sign convention used in this paper is shown in Figure 1, with the *y* component being into the page. In a practical EM system, the receiver coils will rotate in flight. We will assume that the three components of the measured primary field and an assumed bird position have been used to correct for any rotation of the coil.

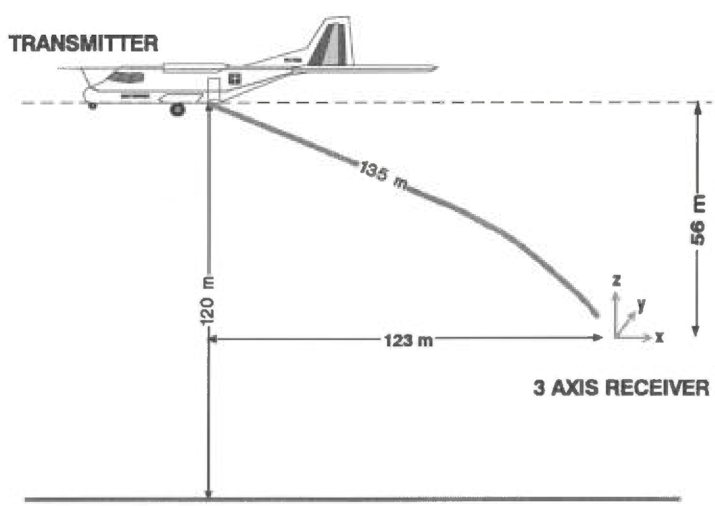

Fig. 1: The geometric configuration of the GEOTEM® system. The system comprises a transmitter on the aircraft and a receiver sensor in a "bird" towed behind the aircraft. The *z* direction is positive up, *x* is positive behind the aircraft, and *y* is into the page (forming a right-hand coordinate system).

SOUNDING IN LAYERED ENVIRONMENTS

In a layered environment, the induced current flow is horizontal (Morrison et al., 1969) so the *z* component of the secondary response (V_z) is much larger than the *x* component (V_x), particularly in resistive ground and/or at late delay times. At the same time, the spheric noise in the *z* direction is 5 to 10 times less than in the horizontal directions (Macnae, 1984; McCracken et al., 1986), so V_z has a greater signal-to-noise ratio. Figure 2 shows theoretical curves over two different, but similar, layered earth models. One model is a half-space of 500 Ω·m and the other is a 350 m thick layer of 500 Ω·m overlying a highly resistive basement. In this plot the data have been normalized by the total primary field. The *z* component (V_z) is 6 to 10 times larger than V_x, and both curves are above the noise level, at least for part of the measured transient. On this plot, a noise level of 30 ppm has been assumed, which would be a typical noise level for both components when the spheric activity is low. To distinguish between the response of the half-space and thick layer, the difference between the response of one model and the response of the other model must be greater than the noise level. Figure 3 shows this difference for both components. Only the V_z difference is above the noise level. Hence for the case shown, V_z is more useful than V_x for determining whether there is a resistive layer at 350 m depth. Because V_z is generally larger in a layered environment, the vertical component will generally be better at resolving the conductivity at depth.

In the above discussion, we have assumed that corrections have been made for the coil rotation. An alternative approach is to calculate and model the magnitude of the total field, as this quantity is independent of the receiver orientation. Macnae et al. (1991) used this strategy when calculating the conductivity depth sections for SPECTREM data.

The symmetry of the secondary field of a layered environment is such that the *y* component response (V_y) will always be zero. In fact, the V_y component will be zero whenever the conductivity structure on both sides of the aircraft is the same. A non-zero V_y is therefore useful in identifying off-line lateral inhomogeneities in the ground.

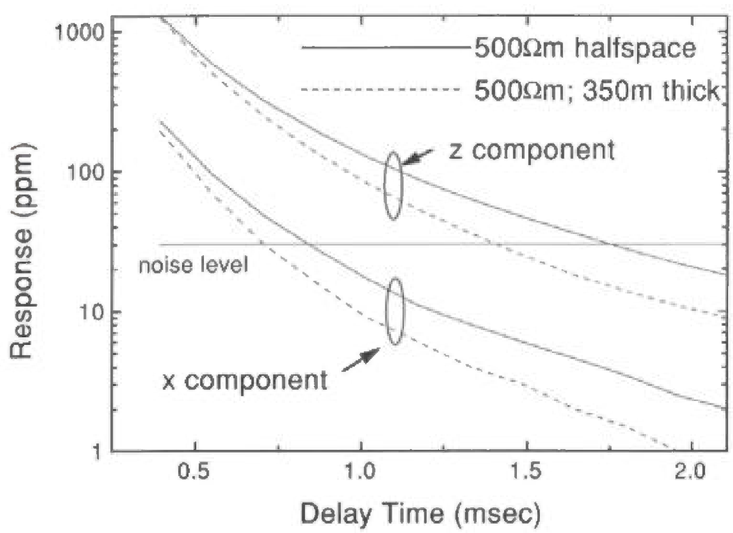

Fig. 2. The response for a 500 Ω·m half-space (solid line) and a 500 Ω·m layer of thickness 350 m overlying a resistive half-space (dashed line). The *z*-component responses are the two curves with the larger amplitudes and the two *x*-component response curves are 6 to 10 times smaller than the corresponding *z* component. A noise level of 30 ppm is considered to be typical of both components in the absence of strong spherics.

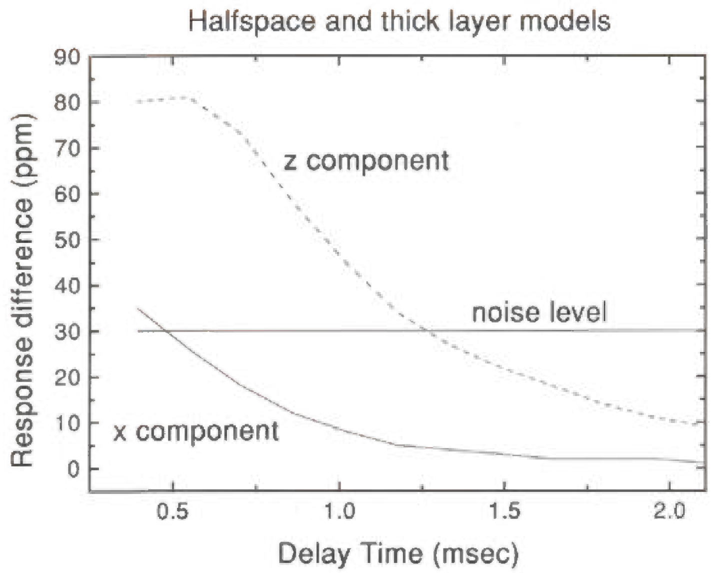

Fig. 3: The difference in the response of each component for the half-space and thick layer models of Figure 2. Only the z-component difference is above the noise level for a significant portion of the transient. Therefore, this is the only component capable of distinguishing between the responses of the two models.

DISCRETE CONDUCTORS

In our discrete conductor study, models have been calculated using a simple plate in free-space model (Dyck and West, 1984) to provide some insight into the geometry of the induced field. The extension to more complex models, such as those incorporating current gathering, will not be considered in this paper.

Historically, airborne transient electromagnetic (TEM) data have been used for conductor detection. The old INPUT system was designed to measure V_x because this component gave a large response when the receiver passed over the top of a vertical conductor. The bottom part of Figure 4 shows the response over a vertical conductor, which has been plotted at the receiver position. The V_x profile (smaller of the two solid lines) has a large peak corresponding with the conductor position. Note that there is also a peak at 200 m, just before the transmitter passes over the conductor, and a trailing edge negative to the left of the conductor. The *z* component (dashed line) has two peaks and a large negative trough just before the conductor. Because of the symmetry, the V_y response (dotted line) is zero.

All the peaks, troughs and negatives make the response of a single conductor complicated to display and hence interpret. The display can be simplified by plotting the "energy envelope" (EE) of the response. This quantity is defined as follows:

$$EE = \sqrt{V_x^2 + \overline{V}_x^2 + V_y^2 + \overline{V}_y^2 + V_z^2 + \overline{V}_z^2},$$

where $\overline{}$ denotes the Hilbert transform of the quantity. The energy envelope plotted on Figure 4 (the larger of the two solid curves) is almost symmetric, and would be a good quantity to present in plan form (as contours or as an image). For flat-lying conductors, the energy envelope has a maximum at the leading edge (just after the aircraft flies onto the conductor).

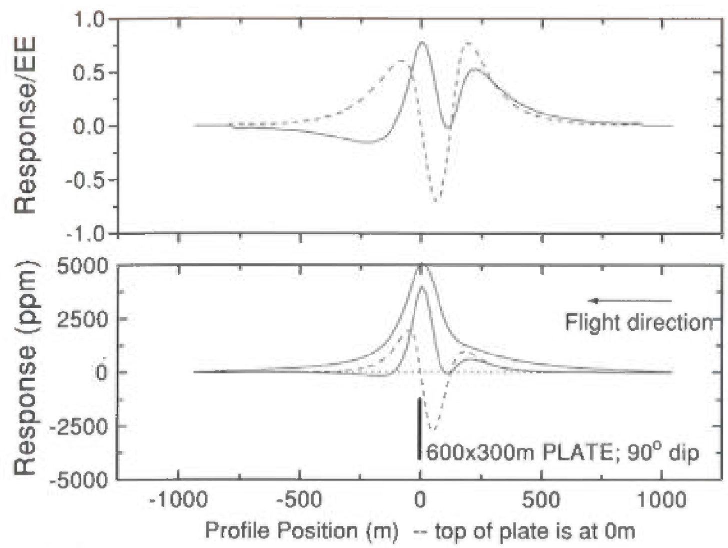

Fig. 4. (Bottom) the response of a 600 by 300 m plate 120 m below an aircraft flying from right to left. The plotting point for the response is below the receiver. The *x*-component response is the smaller amplitude solid line, the *z*-component is the dashed line, and the *y*-component response is the dotted line. The larger amplitude solid line is the "energy envelope" of all three components. (Top) the z and x-components normalized by the energy envelope. These and all subsequent curves are for a delay time of 0.4 ms after the transmitter current is turned off.

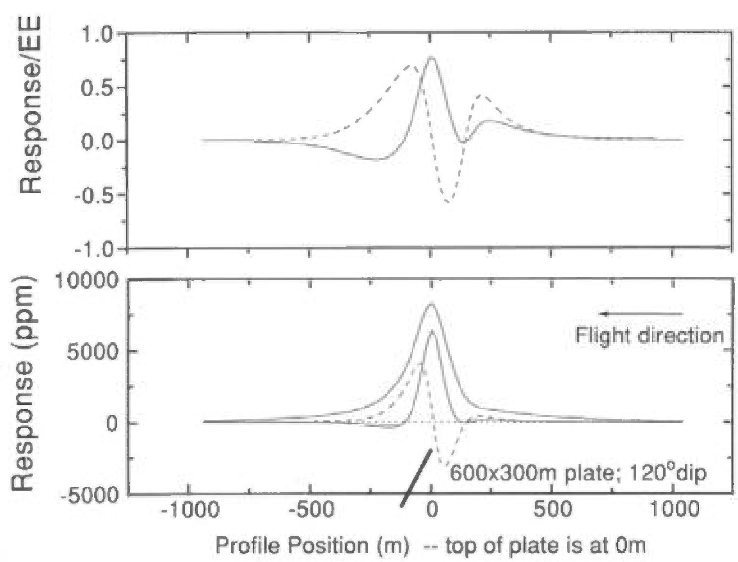

Fig. 5 (Bottom) same as Figure 4, except the plate is now dipping at 120°. On the top graph note the down-dip (left) peak on the normalized *z*-component response is larger than the right peak (c.f. Figure 4).

What little asymmetry remains in the energy envelope is a good indication of the coupling of the AEM system to the conductor. If the response profile for each component is normalized by the energy envelope, then the effect of system coupling will be removed (at least partially) and the profiles will appear more symmetric. For example, the top part of Figure 4 shows the V_x and V_z normalized by the energy envelope at each point. The size of the two *x* peaks and the two *z* peaks are now roughly comparable.

Dip determination

The response of a plate with a dip of 120° is shown on Figure 5. For the V_x/EE and V_z/EE profiles, the peak on the down dip side is larger. For shallow dips, it becomes difficult to identify both V_x/EE peaks, but the two positive V_z/EE peaks remain discernable. Plotting the ratio of the magnitudes of these two V_z/EE peaks, as has been done with solid squares on Figure 6, shows that the ratio is very close to the tangent of the dip divided by 2. Hence, calculating the ratio of the peak amplitudes (R) will yield the dip angle θ using

$$\theta = 2 \tan^{-1}(R).$$

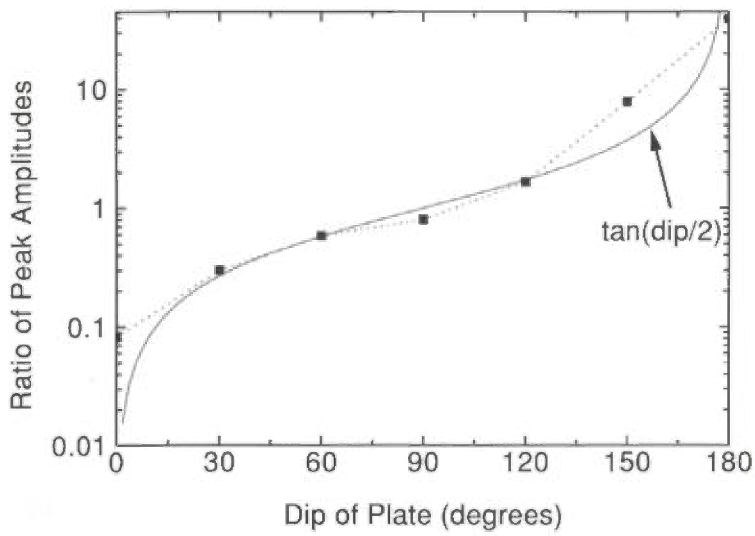

Fig. 6. The ratio of the peak amplitudes of the normalized z-component response (left/right) plotted with solid squares. The ratio plots very close to the tangent of half the dip angle θ of the plate.

Depth Determination

As the depth of the body increases, there is a corresponding increase in the distance between the two positive peaks in the V_z/EE profile. As an example of this, Figure 7 shows the case of a plate 150 m deeper than the plate of Figure 4. The peaks are now 450 m apart, as compared with 275 m on Figure 4. A plot of the peak-to-peak distances for a range of depths is shown on Figure 8 for plates with 60, 90 and 120° dips. Because the points follow a straight line, it can be concluded that for near vertical bodies (60° to 120° dips), the depth to the top of the body *d* can be determined from the measured peak-to-peak distances using the linear relationship depicted in Figure 8. The expected error would be about 25 m. Such an error is tolerable in airborne EM interpretation. More traditional methods for determining *d* analyze the rate of decay of the measured response (Palacky and West, 1973). Our method requires only the V_z/EE response profile at a single delay time. Analyzing this response profile for each delay time allows *d* to be determined as a function of delay time, and hence any migration of the current system in the conductor could be tracked.

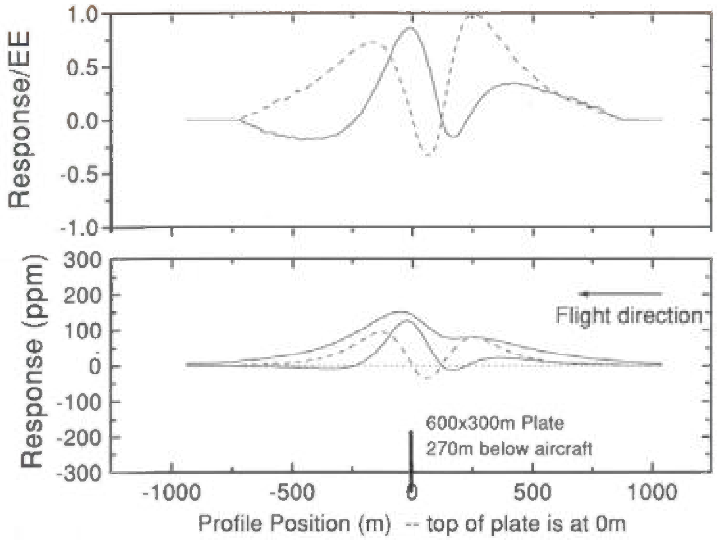

Fig. 7. The same as Figure 4, except the plate is now 270 m below the aircraft. Note that the distance between the z-component peaks is now much greater.

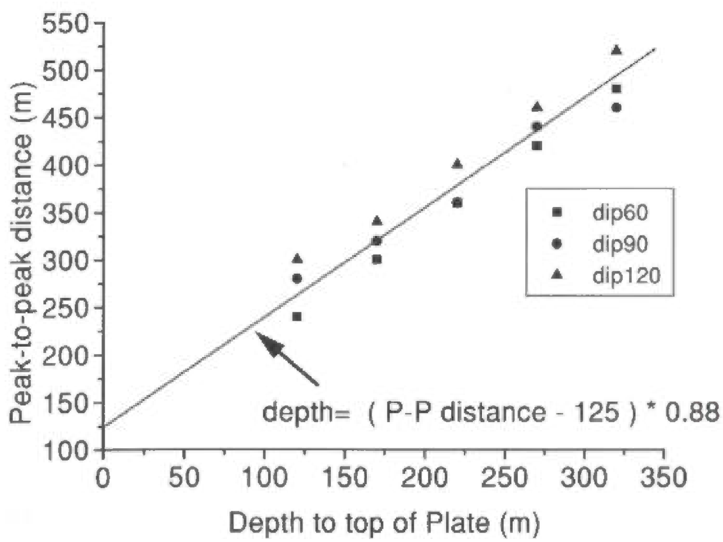

Fig. 8. The peak-to-peak distance as a function of plate depth for three different dip angles θ. A variation in dip of $\pm 30°$ does not result in a large change in the peak to peak distance.

Strike and offset determination

The response shown in Figure 4 varies in cases when the plate has a strike different from 90° or the flight path is offset from the center of the plate.

Figure 9 shows the response for a plate with zero offset and Figure 10 shows the plate when it is offset by 150 m from the profile line. The calculated voltages V_z and V_x are little changed from the no offset case, but the V_y response, is no longer zero. In fact, the shape of the V_y curve appears to be the mirror image of the V_z curve.

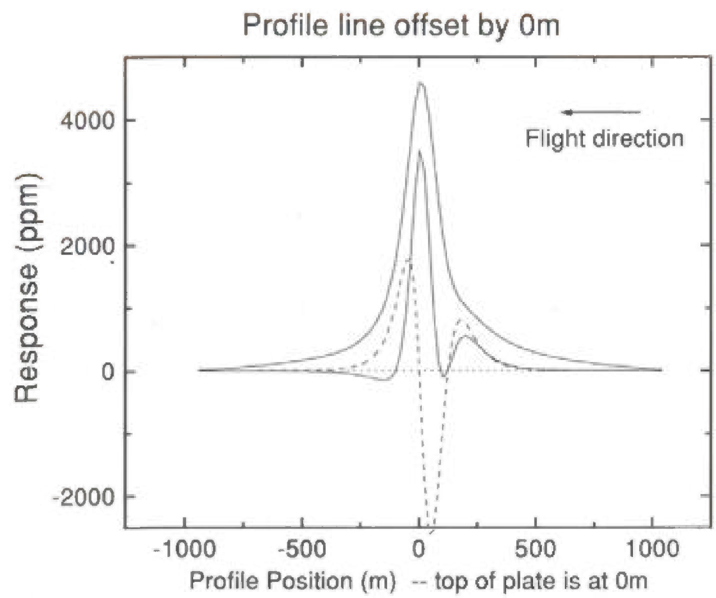

Fig. 9 The response of a 300 by 300 m plate traversed by a profile line crossing the center of the plate in a direction perpendicular to the strike of the plate (the strike angle ζ of the plate with respect to the profile line is 90°).

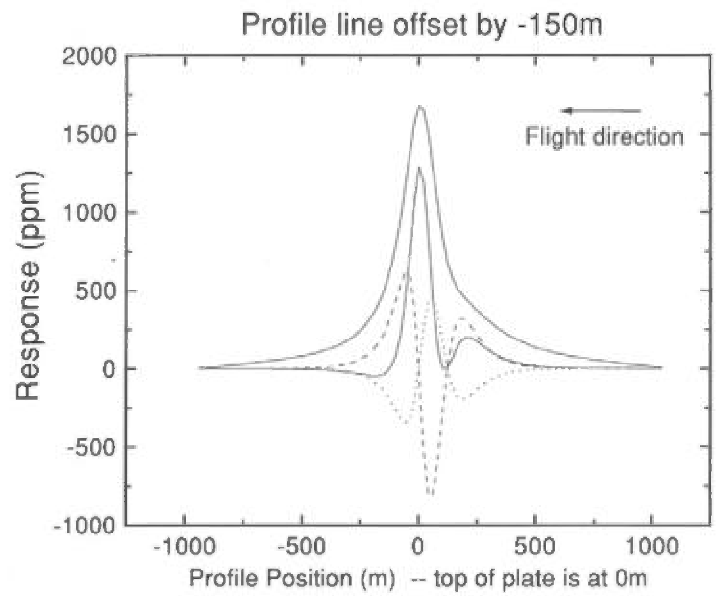

Fig. 10. Same as Figure 9, except the profile line has been offset from the center of the plate by –150 m in the y direction (equivalent to a +150 m displacement of the plate.

In the case when the plate strikes at 45°, the *y* component is similar in shape but opposite in sign to the *x* component response (Figure 11).

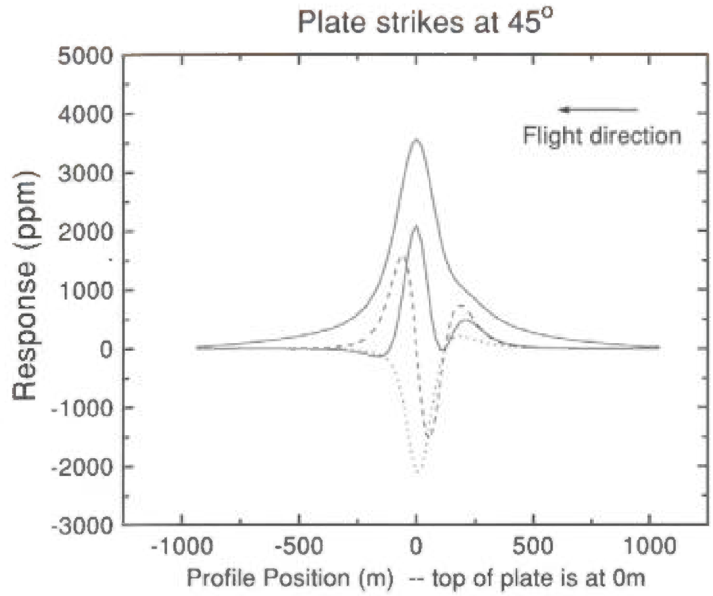

Fig. 11 Same as Figure 9, except the profile line traverses the plate such that the strike angle ζ of the plate with respect to the profile line is 45°.

These similarities can be better understood by looking at schematic diagrams of the secondary field from the plate. Figure 12 shows a plate and the field in section. For zero offsets, the field is vertical (*z* only). As the offset increases, the aircraft and receiver moves to the right and the measured field rotates into the *y* component.

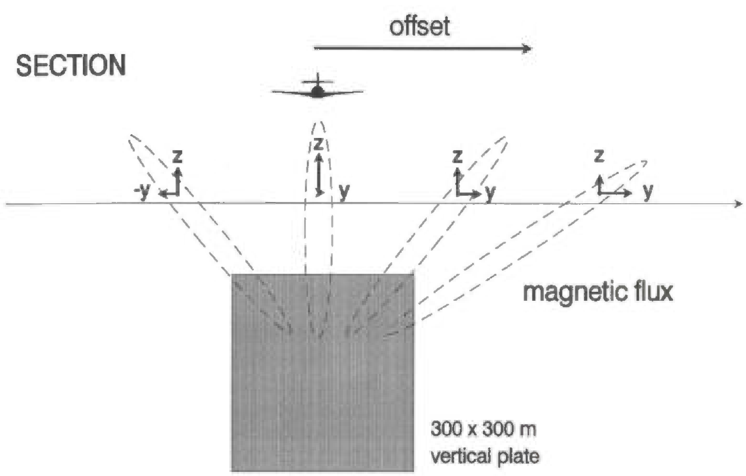

Fig. 12. A schematic diagram of the plate and the magnetic flux of the secondary field (section view). For increasing offset of the aircraft and receiver from the center of the plate, the magnetic field at the receiver rotates from the *z* to the *y* component.

The secondary field is depicted in plan view in Figure 13. Variable strike is simulated by leaving the plate stationary and changing the flight direction. When the strike of the plate is different from 90°, the effective rotation of the EM system means that the secondary field, which was previously measured purely in the *x* direction, is now also measured in the *y* direction.

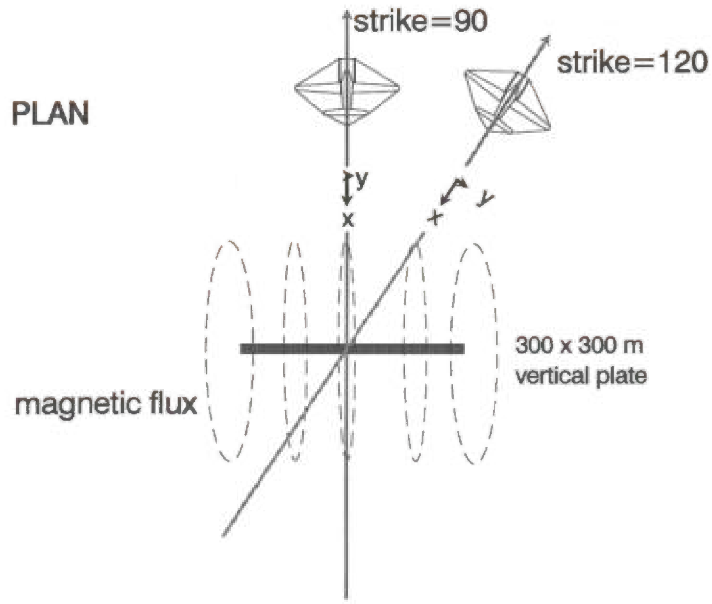

Fig. 13. A schematic diagram of the plate and the magnetic flux of the secondary field (plan view). Here varying strike is depicted by an equivalent variation of the flight direction. As the flight direction rotates from a strike angle of 90°, the receiver rotates so as to measure a greater response in the *y* direction.

The *y* component (V_y) can thus be considered to a be a mixture of V_x and V_z components, viz

$$V_y = C_{stk} V_x + C_{off} V_z ,$$

an equation that is only approximate. The response for a variety of strike angles and offset distances has been calculated and in each case the *y* component response has been decomposed into the *x* and *z* components by solving for the constants of proportionality C_{stk} and C_{off}.

A plot of C_{stk} for the case of zero offset and varying strike direction ξ is seen on Figure 14. The values of C_{stk} determined from the data are plotted with solid squares and compared with the tan(90°- ξ). Because the agreement is so good, the formula

$$\xi = 90 - \tan^{-1} (C_{stk})$$

can be used to determine the strike. This relation was first obtained by Fraser (1972).

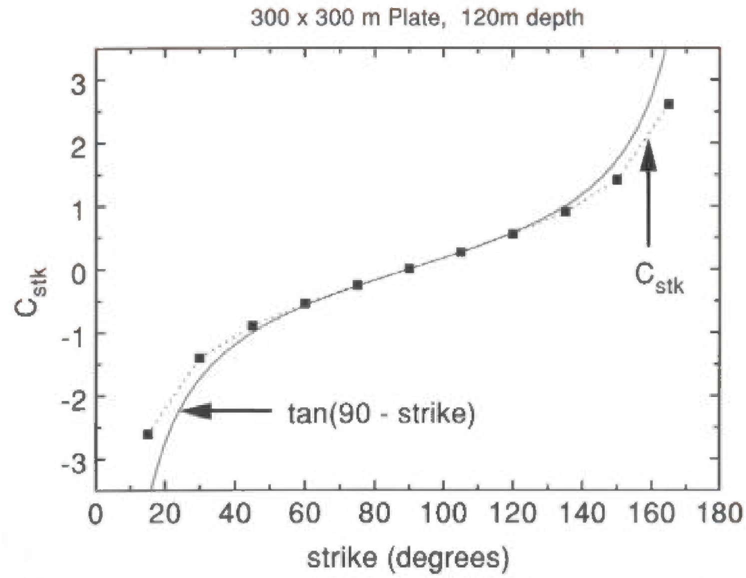

Fig. 14. The ratio $C_{stk} = V_y/V_x$ plotted as a function of varying strike angle (solid squares). The data agree very closely with the cotangent of the ζ.

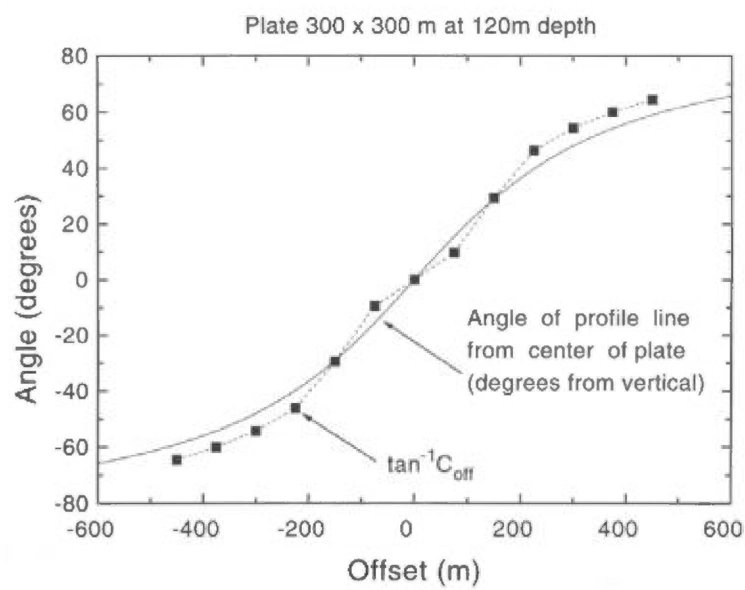

Fig. 15. The arctangent of $C_{off} = V_y/V_z$, plotted as a function of varying offset (solid squares). There is good agreement between this quantity and the angle ϕ between a vertical line and the line from the center of the top edge of the plate to the profile line.

When the strike is fixed at 90°, and the offset varies, the corresponding values obtained for C_{off} have been plotted with solid squares on Figure 15. Again, there is good agreement with the arctangent of C_{off} and the angle ϕ between a vertical line and the line that joins the center of the top edge of the plate with the position where the aircraft traverse crosses the plane containing the plate. If an estimate of the distance to the top of the conductor D is already obtained using the method described above, or by the method described in Palacky and West (1973), then

$$D = \sqrt{(O^2 + d^2)} ,$$

(where d is the depth below surface). Hence, the offset distance O can be written as follows

$$O = d \tan(\phi)$$
$$= d\,C_{off}$$
$$= C_{off}\sqrt{(D^2 - O^2)}$$

which can be rearranged to give

$$O = C_{off}\,D / \sqrt{(1 + C_{off}^2)}.$$

Lateral delectability

Figure 12 illustrates that V_y becomes relatively strong as the lateral displacement from the conductor is increased. Thus, if V_y is measured, then the total signal will remain above the noise level at larger lateral displacements of the traverse line from the conductor. This has been illustrated by assuming a flat-lying conductor, here approximated by a wire-loop circuit of radius 125 m (Figure 16). The *x*, *y* and *z* components of the response have been computed using the formula for the large-loop magnetic fields in Wait (1982). The results are plotted on Figure 17 as a function of increasing lateral displacement *L* of the transmitter/receiver from the center of the conductor. The transmitter and receiver are separated in a direction perpendicular *L* to simulate the case when the system is maximal coupled to the conductor, but the flight line misses the target by an increasing amount. The effect of varying the conductance or measurement time has been removed by normalizing the response to the total response measured when the system is at zero displacement. At displacements greater than 80 m, the *y* component is clearly larger than any other component. Assuming the same sensitivity and noise level for each component (which is a realistic assumption if the data are corrected for coil rotation and the spheric activity is low), it is clearly an advantage to measure V_y, as this will increase the chances of detecting the target when the flight line has not passed directly over the conductor.

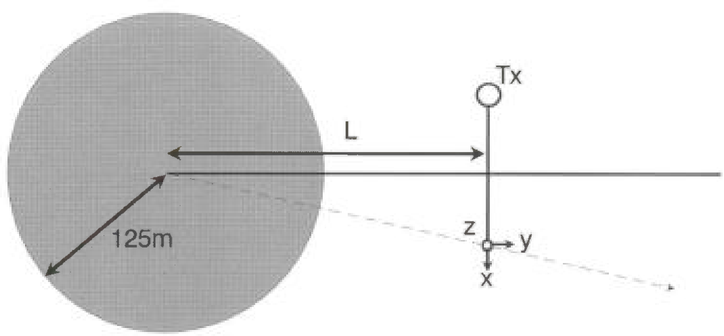

Fig. 16. Plan view of a flat-lying conductor (a circular loop with a radius of 125 m). The AEM system is offset a distance *L* from the center of the conductor in a direction perpendicular to the traverse direction. The traverse direction of the system is from the bottom to the top of the figure.

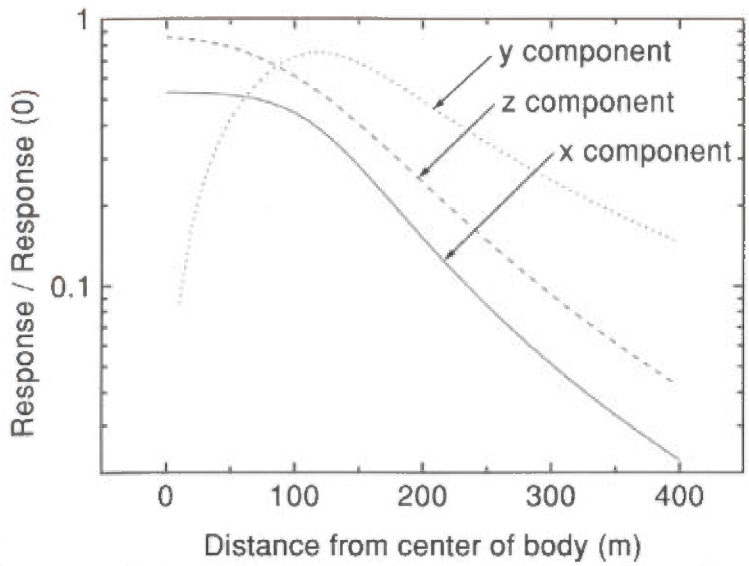

Fig. 17. The normalized response of the EM system plotted as a function of increasing offset distance *L*. The *x* component falls off most rapidly and the y component most slowly with increasing offset distance.

CONCLUSIONS

AEM systems measuring three components of the response can be used to infer more and/or better information than those systems that measure with only one component, i.e., V_x.

The *z* component data enhances the ability of the AEM system to resolve layered structures as the *z* component has a larger signal and a smaller proportion of spheric noise than any other component. If all the components are employed to correct for coil rotation, then the data quality and resolving power is increased further, as individual components are not contaminated by another component. Having better signal-to-noise and greater fidelity in the data will allow deeper layers to be interpreted with confidence.

A non-zero *y* component is helpful in identifying when the conductivity structure has a lateral inhomogeneity that is not symmetric about the flight line.

All components can be used to calculate the energy envelope, which is a valuable quantity to image. The energy envelope has a single peak over a vertical conductor and two peaks over a dipping conductor (one at either end). The asymmetry in the response profile of each individual component can be reduced by normalizing each profile by the energy envelope.

All three components are of great use in determining the characteristics of discrete conductors. For example, the distance between the two positive peaks in the V_z/EE profile can be employed to determine the depth. Also, the ratio of the magnitude of the two V_z/EE peaks helps to ascertain the dip of the conductor. The *x* component has been used in the past for these purposes, but is not as versatile, as it requires the data at all delay times, or an ability to identify a very small peak.

The *y*-component can be utilized to extract information about the conductor that cannot be obtained from single component AEM data. The degree of mixing between the *y* and *z* components can give the lateral offset of the conductor (provided the depth is known), while the mixing between the *y* and *x* component gives the strike of a vertical conductor.

Finally, because the *y* component decreases most slowly with increasing lateral offset, this component gives an enhanced ability to detect a conductor positioned at relatively large lateral distances from the profile line, either between lines or beyond the edge of a survey boundary.

ACKNOWLEDGMENTS

The authors wish to thank Geoterrex for the permission to publish the results of this model study. This paper has been allocated Geological Survey of Canada Contribution No. 36894.

REFERENCES

Annan, A. P., 1986, Development of the PROSPECT I airborne electromagnetic system, in Palacky. G. J., Ed., Airborne resistivity mapping : Geol. Surv. Can. Paper **86-22**, 63-70.

Annan, A. P., and Lockwood, R., 1991, An application of airborne GEOTEM in Australian conditions: Expl., Geophys., **22**, 5-12.

Barnett, C. T., 1984, Simple inversion of time-domain electromagnetic data: Geophysics, **49**, 925-933.

Cull, J. P., 1993, Downhole three component TEM probes: Expl. Geophys., **24**, 437-442.

Dyck, A. V., and West G. F., 1984, The role of simple computer models in interpretations of wide-band, drill-hole electromagnetic surveys in mineral exploration: Geophysics, **49**, 957-980.

Fraser, D. C., 1972, A new multi-coil aerial electromagnetic prospecting system: Geophysics, **37**, 518-537.

Frischknecht, F. C., Labson, V. F., Spies, B. R., and Anderson, W. L., 1991, Profiling methods using small sources, in Nabighian M. N., Ed., Electromagnetic methods in applied geophysics, Vol. 2, Applications: Soc. Expl. Geophys. Investigations in geophysics, no. 3, 105-270.

Hodges, D. G., Crone, J. D., and Pemberton, R., 1991, A new multiple component downhole pulse EM probe for directional interpretation: Proc. 4th Int. MGLS/KEGS Sym. on Borehole Geophys. For Min. Geotech. And Groundwater Appl.

Hogg, R. L. S., 1986, The Aerodat multigeometry, broadband transient helicopter electromagnetic system, in Palacky. G. J., Ed., Airborne resistivity mapping: Geol. Surv. Can. Paper **86-22**, 79-89.

Lee, J., 1986, A three component drill-hole EM receiver probe: M.Sc. thesis, Univ. of Toronto.

Macnae, J. C., 1984, Survey design for multi-component electromagnetic systems: Geophysics, **49**, 265-273.

Macnae, J. C., Smith, R. S., Polzer, B. D., Lamontagne, Y., and Klinkert, P. S., 1991, Conductivity-depth imaging of airborne electromagnetic step-response data: Geophysics, **56**, 102-114.

McCracken, K. G., Oristaglio, M. L., and Hohmann, G. W., 1986, Minimization of noise in electromagnetic exploration systems: Geophysics, **51**, 819-132.

McNeill, J.D., and Labson, V., 1991, Geological mapping using VLF radio fields, in Nabighian M. N., Ed., Electromagnetic methods in applied geophysics, Vol. 2, Applications: Soc. Expl.

Geophys. Investigations in geophysics, no. 3, 521-640.

Morrison, H.F., Phillips, R.J., and O'Brien, D.P., 1969, Quantitative interpretation of transient electromagnetic fields over a layered earth: Geophys. Prosp. **17**, 82-101.

Palacky, G. J., and West, G. F., 1973, Quantitative measurements of Input AEM measurements: Geophysics, **38**, 1145-1158.

Palacky, G. J., and West, G. F., 1991, Airborne electromagnetic methods, in Nabighian M. N., Ed., Electromagnetic methods in applied geophysics, Vol. 2, Applications: Soc. Expl. Geophys. Investigations in geophysics, no. 3, 811-879.

Spies, B. R., and Frischknecht, F. C., 1991, Electromagnetic sounding, in Nabighian M. N., Ed., Electromagnetic methods in applied geophysics, Vol. 2, Applications: Soc. Expl. Geophys. Investigations in geophysics, no. 3, 285-425.

Vozoff, K., 1990, Magnetotellurics: Principles and practices: Proc. Indian Acad. Sci., **99**, 441-471.

Vozoff, K., 1991, The magnetotelluric method, in Nabighian M. N., Ed., Electromagnetic methods in applied geophysics, Vol. 2, Applications: Soc. Expl. Geophys. Investigations in geophysics, no. 3, 641-711.

Wait, J. R., 1982, Geo-electromagnetism: Academic Press Inc.

Zonge K. L., and Hughes, L. J., 1991, Controlled-source audio-magnetotellurics, in Nabighian M. N., Ed., Electromagnetic methods in applied geophysics, Vol. 2, Application: Soc. Expl. Geophys. Investigations in geophysics, no. 3, 713-809.

Appendix E

Data Archive Description

Data Archive Description:

Survey Details

Survey Area Name:	Deborah Lake Property
Job number:	10408
Client:	Western Troy Capital Resources Inc.
Survey Company Name:	Fugro Airborne Surveys
Flown Dates:	December 10th – December 11th, 2010
Archive Creation Date:	January, 2011

Survey Specifications

Traverse Line Azimuth:	045º-225º
Traverse Line Spacing:	200 m
Traverse Line Spacing (infill):	100 m
Flying Elevation:	120 m Mean Terrain Clearance
Average Aircraft Speed:	65 m/s

Geodetic Information for map products

Projection:	Universal Transverse Mercator
Datum:	NAD83
Central meridian:	63° West
False Easting:	500000 metres
False Northing:	0 metres
Scale factor:	0.9996
UTM Zone:	20 North

Equipment Specifications:

Navigation

GPS Receiver:	NovAtel OEM4, 12 Channels
Aircraft:	Casa (Twin Turbo Propeller)
Video Camera:	Panasonic WV-CL302

Electromagnetics

Type:	GEOTEM®, 30 channel multi-coil system
Installation:	Vertical axis loop (231m^2 area with 6 turns) mounted on aircraft Receiver coils in a towed bird.
Coil Orientation:	X, Y and Z
Frequency:	30 Hz
Pulse width:	4044µs
Off-time:	12599µs
Geometry:	Tx-Rx horizontal separation of ~125 m Tx-Rx vertical separation of ~47m
Sampling:	0.25 s

Data Windows:

Channel	Start (p)	End (p)	Width (p)	Start (ms)	End (ms)	Width (ms)	Mid (ms)
1	4	18	15	0.024	0.146	0.122	0.085
2	19	176	158	0.146	1.432	1.286	0.789
3	177	333	157	1.432	2.710	1.278	2.071
4	334	491	158	2.710	3.996	1.286	3.353
5	492	507	16	3.996	4.126	0.130	4.061
6	508	512	5	4.126	4.167	0.041	4.146
7	513	518	6	4.167	4.215	0.049	4.191
8	519	526	8	4.215	4.281	0.065	4.248
9	527	536	10	4.281	4.362	0.081	4.321
10	537	548	12	4.362	4.460	0.098	4.411
11	549	562	14	4.460	4.574	0.114	4.517
12	563	578	16	4.574	4.704	0.130	4.639
13	579	596	18	4.704	4.850	0.146	4.777
14	597	616	20	4.850	5.013	0.163	4.932
15	617	641	25	5.013	5.216	0.203	5.115
16	642	671	30	5.216	5.461	0.244	5.339
17	672	706	35	5.461	5.745	0.285	5.603
18	707	746	40	5.745	6.071	0.326	5.908
19	747	791	45	6.071	6.437	0.366	6.254
20	792	841	50	6.437	6.844	0.407	6.641
21	842	901	60	6.844	7.332	0.488	7.088
22	902	971	70	7.332	7.902	0.570	7.617
23	972	1051	80	7.902	8.553	0.651	8.228
24	1052	1141	90	8.553	9.285	0.732	8.919
25	1142	1241	100	9.285	10.099	0.814	9.692
26	1242	1361	120	10.099	11.076	0.977	10.588
27	1362	1501	140	11.076	12.215	1.139	11.646
28	1502	1661	160	12.215	13.517	1.302	12.866
29	1662	1841	180	13.517	14.982	1.465	14.250
30	1842	2048	207	14.982	16.667	1.685	15.824

ASCII and Geosoft Line Archive File Layout (Deborah_Lake_ascii.xyz & Deborah_Lake.gdb):

Field	Variable	Description	Units
1	line	Line Number	line+part
2	fiducial	Universal Time (Seconds Since Midnight)	sec.
3	flight	Flight Number	-
4	date	Date of the Survey Flight	yymmdd
5	lat_nad83	Latitude in NAD83	degrees
6	long_nad83	Longitude in NAD83	degrees
7	x_nad83	Easting (X) in NAD83 UTM Zone 20N	m
8	y_nad83	Northing (Y) in NAD83 UTM Zone 20N	m
9	gpsz	GPS Elevation (Referenced to Mean Sea Level)	m
10	alt_radar	Radar Altimeter	m
11	dtm	Terrain (Referenced to Mean Sea Level)	m
12	primary_field	Electromagnetic X-Coil Primary Field	µV
13	hz_monitor	Powerline Monitor (60 Hz)	µV
14-18	x_ontime	Final dB/dt X-Coil Channels 01 to 05	pT/s
19-43	x_offtime	Final dB/dt X-Coil Channels 06 to 30	pT/s
44-48	y_ontime	Final dB/dt Y-Coil Channels 01 to 05	pT/s
49-73	y_offtime	Final dB/dt Y-Coil Channels 06 to 30	pT/s
74-78	z_ontime	Final dB/dt Z-Coil Channels 01 to 05	pT/s
79-103	z_offtime	Final dB/dt Z-Coil Channels 06 to 30	pT/s
104-108	Bx_ontime	Final B-Field X-Coil Channels 01 to 05	fT
109-133	Bx_offtime	Final B-Field X-Coil Channels 06 to 30	fT
134-138	By_ontime	Final B-Field Y-Coil Channels 01 to 05	fT
139-163	By_offtime	Final B-Field Y-Coil Channels 06 to 30	fT
164-168	Bz_ontime	Final B-Field Z-Coil Channels 01 to 05	fT
169-193	Bz_offtime	Final B-Field Z-Coil Channels 06 to 30	fT
194-198	raw_x_ontime	Raw dB/dt X-Coil Channels 01 to 05	pT/s
199-223	raw_x_offtime	Raw dB/dt X-Coil Channels 06 to 30	pT/s
224-228	raw_y_ontime	Raw dB/dt Y-Coil Channels 01 to 05	pT/s
229-253	raw_y_offtime	Raw dB/dt Y-Coil Channels 06 to 30	pT/s
254-258	raw_z_ontime	Raw dB/dt Z-Coil Channels 01 to 05	pT/s
259-283	raw_z_offtime	Raw dB/dt Z-Coil Channels 06 to 30	pT/s
284-288	raw_Bx_ontime	Raw B-Field X-Coil Channels 01 to 05	fT
289-313	raw_Bx_offtime	Raw B-Field X-Coil Channels 06 to 30	fT
314-318	raw_By_ontime	Raw B-Field Y-Coil Channels 01 to 05	fT
319-343	raw_By_offtime	Raw B-Field Y-Coil Channels 06 to 30	fT
344-348	raw_Bz_ontime	Raw B-Field Z-Coil Channels 01 to 05	fT
349-373	raw_Bz_offtime	Raw B-Field Z-Coil Channels 06 to 30	fT
374	tauBx10_30	Tau of B-Field X-Coil Channels 10-30	µs
375	cond_ts_z01	Equivalent Delay Time Conductance of dB/dT Z-Coil Channel 01	mS
376	momz2	Second Order Moment of B-Field Z-Coil	ppm

Note – The null values in the ASCII archive are displayed as *

Grid Archive File Description:

The grids are in Geosoft format. A grid cell size of 50 m was used for all area grids.

File	Description	Units
Deborah_Lake_tauBx10_30.grd	Tau of B-Field Z-Coil Channels 10-30	µs
Deborah_Lake_cond_ts_z01.grd	Equivalent Delay Time Conductance of dB/dt Z-Coil Channel 01	mS
Deborah_Lake_momz2.grd	Second Order Moment of B-Field Z-Coil	ppm

Appendix F

Map Product Grids

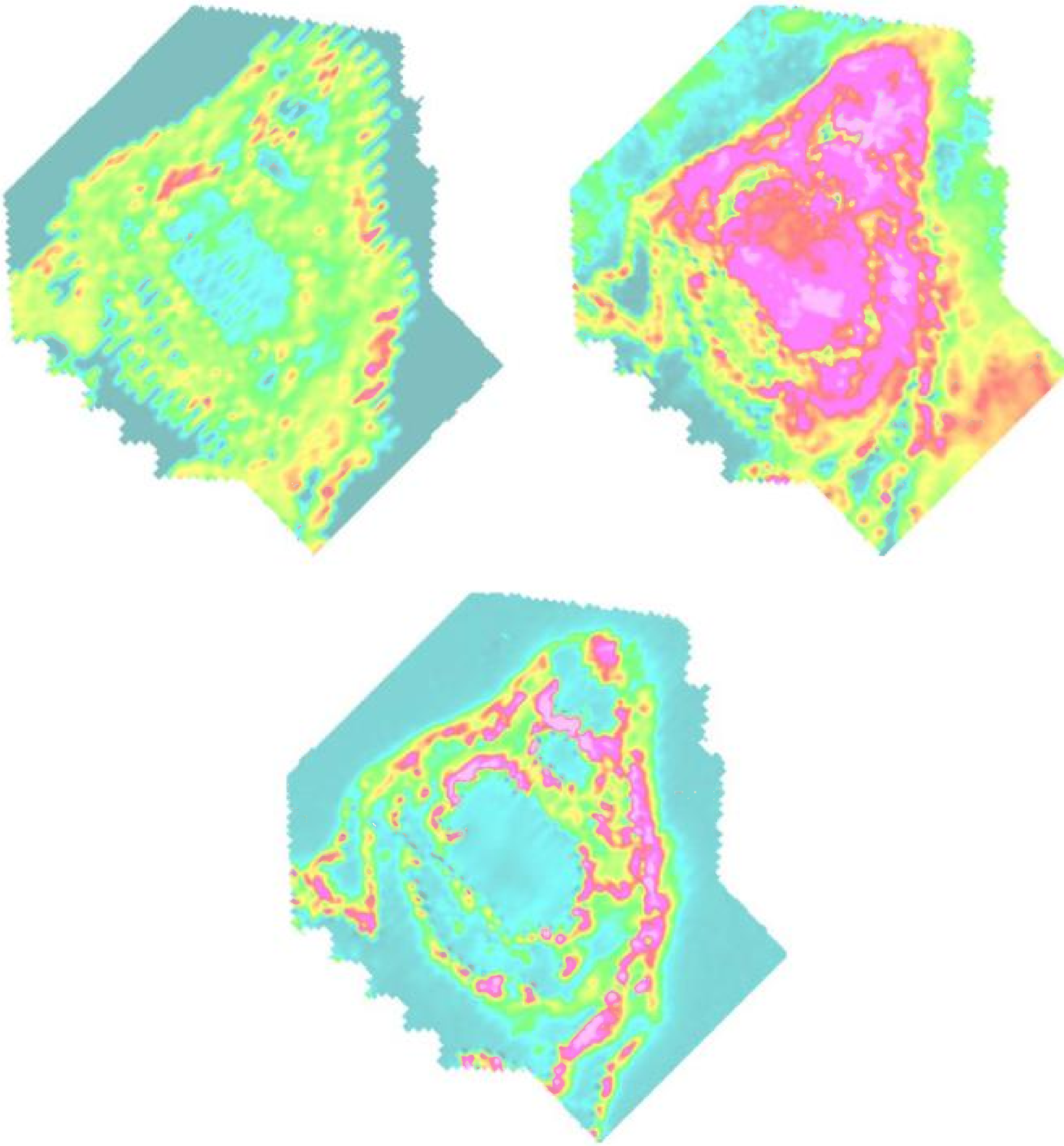

Figure 1. Decay Constant (top left), Equivalent Delay Time Conductance (top right) and Second Order Moment (bottom)

Appendix G

Reference Waveform

Reference Waveform Descriptor:

The information shown is only an example. The actual reference waveforms are provided on CD-ROM or DVD and will have been renamed to ptaFLTpre.out, "FLT" represents the flight number.

The reference waveform can be divided into four main sections, which are described below.

Section 1

This section contains the name of the raw reference waveform file (i.e. D0050704.002). The approximate horizontal and vertical offsets (i.e. 125 m and 50 m) of the EM bird position in meters are listed. These are followed by the base frequency (i.e. 90Hz) in Hertz and the sample interval (i.e. 8.14 μs) in microseconds.

```
GEOTEM Calibration Data - Version 31 July 1998
 'D0050704.002' = Name of original saved parameter table file
      125.000000000000000 = Horizontal TX-RX separation in meters
       50.000000000000000 = Vertical   TX-RX separation in meters
       90.000000000000000 = Base Frequency in Hertz
        8.1380208 = Sample Interval in micro-seconds
```

Section 2

This section displays the gate configuration for channels 1 to 30.

30 Time Gates: First and Last Sample number, RMS chart position:

Start & end samples of each channel

Channels 1 to 30

1	4	18	1
2	19	176	2
3	177	333	3
4	334	491	4
5	492	507	5
6	508	512	6
7	513	518	7
8	519	526	8
9	527	536	9
10	537	548	10
11	549	562	11
12	563	578	12
13	579	596	13
14	597	616	14
15	617	641	15
16	642	671	16
17	672	706	17
18	707	746	18
19	747	791	19
20	792	841	20
21	842	901	21
22	902	971	22
23	972	1051	23
24	1052	1141	24
25	1142	1241	25
26	1242	1361	26
27	1362	1501	27
28	1502	1661	28
29	1662	1841	29
30	1842	2048	30

Section 3

This section contains the different types of conversion factors for each of the components. If the data are provided in ppm the standard procedure is to normalize the data based on the individual components. Three different conversion factors are provided. The first factor converts the data to ppm based on the peak voltages of each individual component. The second factor converts the data to ppm based on the "total" peak voltage, which is actually the RMS value of the 3 components. The third factor converts each component to standard SI units, which are Teslas per second for the dB/dt data and Teslas for the B-field data.

Component:	dBx/dt	dBy/dt	dBz/dt	Bx	By	Bz
IndivPPM_per_DataUnit:	0.1112428E-01	1.106797	0.2890714E-01	0.1519028E-01	1.670836	0.3945841E-01
TotalPPM_per_DataUnit:	0.1038160E-01	0.1038160E-01	0.1038160E-01	0.1417559E-01	0.1417559E-01	0.1417559E-01
SI_Units_per_DataUnit:	0.1000000E-11	0.1000000E-11	0.1000000E-11	0.1000000E-14	0.1000000E-14	0.1000000E-14

Section 4

The last section contains the reference waveform. Each column represents a component (i.e. dBx/dt). The data units (i.e. pT/s) for each component are displayed in the second row. The first column is the sample number. The transmitter channel (TX) values have been converted to transmitter moment value (transmitter current x loop area x number of turns)

For this example there are 2048 samples.

Component:	TX	dBx/dt	dBy/dt	dBz/dt	Bx	By	Bz
DataUnits:	Am^2	pT/s	pT/s	pT/s	fT	fT	fT

2048 Samples:

1	1161.572	38526.84	924.7899	14929.63	-164386.1	447.8830	-57789.91
2	1182.870	37266.81	431.6681	14992.79	-162768.6	466.6186	-57139.19
3	2471.644	130950.8	4966.128	46394.08	-157085.0	682.1624	-55125.55
4	18579.32	3142793.	4921.018	1117837.	-20679.01	895.7482	-6608.309

2045	-1089.137	-41458.52	-304.3134	-15670.09	166886.3	-413.2204	58736.67
2046	-1000.563	-40324.45	-44.37050	-14808.83	165136.1	-415.1462	58093.93
2047	-1006.226	-39601.37	61.07057	-14660.24	163417.3	-412.4956	57457.63
2048	-1134.029	-39423.19	-546.7703	-15091.65	161706.2	-436.2269	56802.61

CERTIFICATE OF REVIEWER

I, Marc A. Vallée, do hereby certify that :

1. I am employed as Senior Geophysicist for the geophysical survey firm Fugro Airborne Surveys Corp.
2. I hold the following academic qualifications: B.Sc.A. Geological Eng. (1978), Laval University, M.Sc. Geophysics (1981), U. of Toronto, Ph.D. Geophysics (1991), École Polytechnique.
3. I am a member in good standing of the Ordre des ingénieurs du Québec (OIQ), member # 36436.
4. I have worked as geophysicist for 25 years.
5. I have had no prior involvement with the Property that forms the subject of this Report.
6. I am not aware of any material fact or material change with respect to the subject matter of the Report that is not reflected in the Report, the omission to disclose which makes the Report misleading.
7. I have reviewed the Report titled "LOGISTICS AND PROCESSING REPORT, GEOTEM® Airborne Electromagnetic Survey, Deborah Lake Property, Québec", dated January 2011 and prepared for Western Troy Capital Resources Inc.

Dated this 7th Day of February, 2011.

Respectfully Submitted

Marc A. Vallée, ing.

Marc A. Vallée, Ph.D., ing.
Senior Geophysicist, Fugro Airborne Surveys Corp.

INGÉNIEUR - ENGINEER
Marc A. Vallée
36436
QUÉBEC